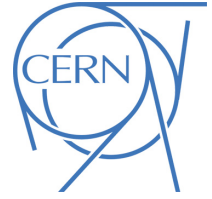




ATLAS CONF Note

ATLAS-CONF-2020-046

14th August 2020



Search for new phenomena in events with two opposite-charge leptons, jets and missing transverse momentum in pp collisions at $\sqrt{s} = 13$ TeV with the ATLAS detector

The ATLAS Collaboration

The results of a search for direct pair production of top squarks and for dark matter in events with two opposite-charge leptons (electrons or muons), jets and missing transverse momentum are reported, using 139 fb^{-1} of integrated luminosity from proton–proton collisions at $\sqrt{s} = 13$ TeV, collected by the ATLAS detector at the Large Hadron Collider during Run-2 (2015-2018). This analysis considers the pair production of top squarks and is sensitive across a wide range of mass differences between the \tilde{t} and lightest neutralino $\tilde{\chi}_1^0$. Additionally, spin-0 mediator dark matter models are considered, in which the mediator is produced in association with a pair of top quarks. The mediator subsequently decays to a pair of dark-matter particles. No significant excess of events is observed above the Standard Model background, and limits are set at 95% confidence level. The results exclude \tilde{t} masses up to about 1 TeV, and $\tilde{\chi}_1^0$ masses up to about 500 GeV. Limits on Dark Matter production are set for scalar (pseudoscalar) mediator masses up to about 250 (300) GeV.



1 Introduction

The Standard Model (SM) of particle physics is extremely successful in describing the phenomena of elementary particles and their interactions and its predictive power has been proven with high precision by particle accelerator experiments. However, despite its success, theoretical and experimental arguments suggest that it is only a low-energy realisation of a more general theory. Several important questions remain unanswered within the SM, such as the nature of dark matter [1, 2], the baryon asymmetry of the universe and the stabilisation of the Higgs boson mass against radiative corrections from the Planck scale. Some of these shortcomings could find an elegant solution with the existence of new particles at the TeV scale, and this motivates extensive searches at the Large Hadron Collider (LHC).

Supersymmetry (SUSY) [3–8] is one of the most promising theories beyond the SM. SUSY is a space-time symmetry that for each SM particle postulates the existence of a partner particle whose spin differs by one-half unit. To avoid the violation of the baryon (B) and lepton (L) numbers, the conservation of the multiplicative quantum number R -parity [9], defined as $R = (-1)^{3(B-L)+2S}$, is assumed. In the framework of a generic R -parity-conserving Minimal Supersymmetric Standard Model (MSSM) [10, 11], SUSY particles are produced in pairs, and the lightest supersymmetric particle (LSP) is stable and a candidate for dark matter [1, 2]. The scalar partners of right-handed and left-handed quarks (squarks), \tilde{q}_R and \tilde{q}_L , can mix to form two mass eigenstates, \tilde{q}_1 and \tilde{q}_2 , with \tilde{q}_1 defined to be the lighter one. In the case of the supersymmetric partner of the top quark, \tilde{t} , large mixing effects can lead to one top squark mass eigenstate, \tilde{t}_1 , that is significantly lighter than the other squarks. The charginos and neutralinos are mixtures of the bino, winos and Higgsinos that are superpartners of the $U(1)$ and $SU(2)$ gauge bosons and the Higgs bosons, respectively. Their mass eigenstates are referred to as $\tilde{\chi}_i^\pm$ ($i = 1, 2$) and $\tilde{\chi}_j^0$ ($j = 1, 2, 3, 4$) in order of increasing masses. In a large variety of models, the LSP is the lightest neutralino $\tilde{\chi}_1^0$.

Despite the fact that the nature and properties of dark matter (DM) remain largely unknown, a range of astrophysical observations provide strong evidence for its existence. It appears as a non-baryonic non-luminous and non-interacting component of the universe mass [12, 13] and one of the candidates for a DM particle is a weakly interacting massive particle (WIMP) [14]. At the Large Hadron Collider, one can search for WIMP DM (χ) pair production in proton–proton collisions. WIMP DM doesn’t interact with the detector leading to signatures with missing transverse momentum. Some simplified benchmark models [15–17] for DM production assume the existence of a mediator particle which couples both to the SM and to the dark sector [18–20]. The couplings of the mediator to the SM fermions are severely restricted by precision flavour measurements. An ansatz that automatically relaxes these constraints is Minimal Flavour Violation [21]. This assumption implies that the interaction between any new neutral spin-0 state and SM matter is proportional to the fermion masses via Yukawa-type couplings¹. It follows that colour-neutral mediators would be largely produced through loop-induced gluon fusion or in association with heavy-flavour quarks.

Searches for direct pair production of the top squark and DM particles in final states with two opposite electric charged leptons (electrons or muons), jets and missing transverse momentum are reported in this paper. The searches exploit the 139 fb^{-1} of proton-proton collision data collected by the ATLAS experiment during Run-2 (2015–2018) at a centre-of-mass energy $\sqrt{s} = 13 \text{ TeV}$. The top squark is assumed to decay into the lightest neutralino. Depending on the mass difference between the top squark and the

¹ Following Ref. [19], couplings to W and Z bosons, as well as explicit dimension-4 $\phi - h$ or $a - h$ couplings, are set to zero in this simplified model. In addition, the coupling of the mediator to the dark sector are not taken to be proportional to the mass of the DM candidates.

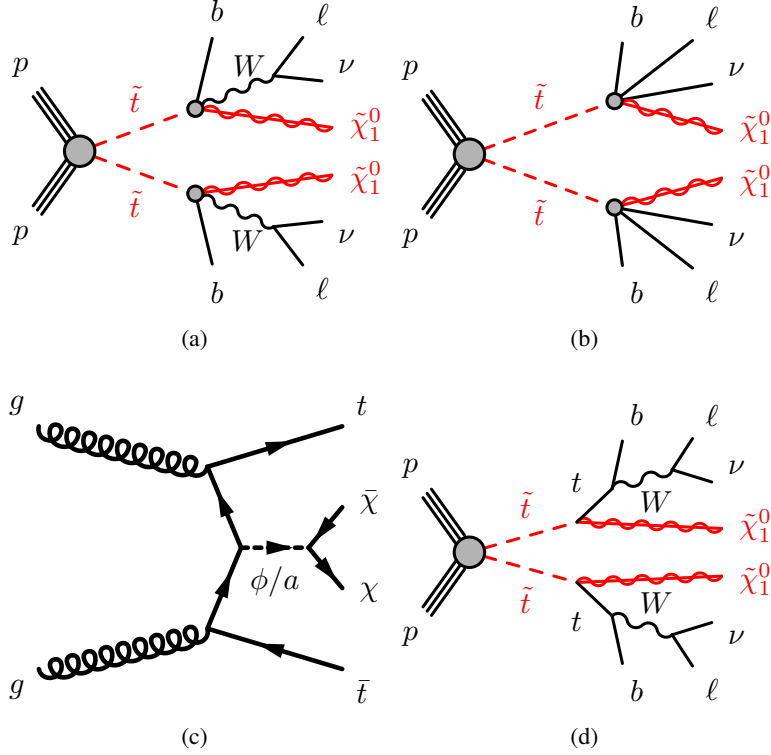


Figure 1: Diagrams representing the signal models targeted by the analyses: (a) the three-body \tilde{t}_1 decay mode into an on-shell W boson, a b -quark and the lightest neutralino ($\tilde{t}_1 \rightarrow bW\tilde{\chi}_1^0$), (b) the four-body \tilde{t}_1 decay mode ($\tilde{t}_1 \rightarrow b\ell\nu\tilde{\chi}_1^0$) where ℓ and ν are a lepton with its neutrino, (c) the spin-0 mediator models, where the mediator decays into a pair of dark-matter particles and is produced in association with a pair of top quarks ($pp \rightarrow \chi\bar{\chi}t\bar{t}$) and (d) the two-body \tilde{t}_1 decay into an on-shell top quark and the lightest neutralino ($\tilde{t}_1 \rightarrow t\tilde{\chi}_1^0$).

lighter SUSY particles, different decay modes are relevant. For $m(W) + m(b) < m(\tilde{t}_1) - m(\tilde{\chi}_1^0) < m(t)$, the three-body decay through an off-shell top quark $\tilde{t}_1 \rightarrow bW\tilde{\chi}_1^0$ occurs (Figure 1(a)). For smaller mass differences, i.e. $m(\tilde{t}_1) - m(\tilde{\chi}_1^0) < m(W) + m(b)$, the four-body decay channel $\tilde{t}_1 \rightarrow bf f'\tilde{\chi}_1^0$, where f and f' are two fermions from the off-shell (W^*) decay, is assumed to occur (Figure 1(b)). In this search, f and f' are a lepton and its associated neutrino. For each of these two decay modes a dedicated event selection is performed to maximise the sensitivity. These selections are referred to as *three-body* and *four-body* selections in this paper.

This paper considers also DM produced in association with top quarks (Figure 1(c)). The DM particles are pair produced through the exchange of a spin-0 mediator, which can be a colour-neutral scalar or pseudoscalar particle (denoted by ϕ or a , respectively), in association with a top quark pair: $pp \rightarrow \chi\bar{\chi}t\bar{t}$. In addition, given the similar final state, the results from the latter selection are also interpreted in scenario with a direct pair production of top squarks which decay into an on-shell top quark and the lightest neutralino $\tilde{t}_1 \rightarrow t\tilde{\chi}_1^0$, with the assumption of $m(\tilde{t}_1) - m(\tilde{\chi}_1^0) > m(t)$ (Figure 1(d)). This last selection is referred as *two-body* selection in this paper.

This paper extends and completes previous ATLAS searches for top squarks and dark matter published using 36 fb⁻¹ collected during 2015 and 2016 Runs [22, 23]. Improvements in sensitivity are obtained using a new discriminating variable, called "object-based E_T^{miss} significance" [24] and exploiting the full

Run-2 dataset. Further increase in sensitivity in the four-body selection is achieved by lowering the leptons' p_T threshold and optimising a dedicated selection to target signal models with a mass difference between \tilde{t}_1 and $\tilde{\chi}_1^0$ of the order of 20 GeV. Previous searches have been performed by both the ATLAS [25–32] and CMS [33–42] collaborations.

After a description of the ATLAS detector in Section 2, the data and simulated Monte Carlo (MC) samples used in the analysis are detailed in Section 3 and the object identification is documented in Section 4. The search strategy, the SM background estimations, the systematic uncertainties are discussed in Sections 5, 6 and 7. The results and their statistical interpretations are presented in Sections 8 and 9. Finally, Section 10 presents the conclusions.

2 ATLAS detector

The ATLAS detector [43] at the LHC covers nearly the entire solid angle around the collision point.² It consists of an inner tracking detector surrounded by a thin superconducting solenoid, electromagnetic and hadronic calorimeters, and a muon spectrometer incorporating three large superconducting toroidal magnets. The inner-detector system (ID) is immersed in a 2 T axial magnetic field and provides charged-particle tracking in the range $|\eta| < 2.5$.

The high-granularity silicon pixel detector covers the vertex region and typically provides four measurements per track, the first hit being normally in the insertable B-layer (IBL) installed before Run 2 [44, 45]. It is followed by the silicon microstrip tracker (SCT) which usually provides eight measurements per track. These silicon detectors are complemented by the transition radiation tracker (TRT), which enables radially extended track reconstruction up to $|\eta| = 2.0$. The TRT also provides electron identification information based on the fraction of hits (typically 30 in total) above a higher energy-deposit threshold corresponding to transition radiation.

The calorimeter system covers the pseudorapidity range $|\eta| < 4.9$. Within the region $|\eta| < 3.2$, electromagnetic calorimetry is provided by barrel and endcap high-granularity lead/liquid-argon (LAr) calorimeters, with an additional thin LAr presampler covering $|\eta| < 1.8$, to correct for energy loss in material upstream of the calorimeters. Hadronic calorimetry is provided by the steel/scintillating-tile calorimeter, segmented into three barrel structures within $|\eta| < 1.7$, and two copper/LAr hadronic endcap calorimeters. The solid angle coverage is completed with forward copper/LAr and tungsten/LAr calorimeter modules optimised for electromagnetic and hadronic measurements respectively.

The muon spectrometer (MS) comprises separate trigger and high-precision tracking chambers measuring the deflection of muons in a magnetic field generated by superconducting air-core toroids. The field integral of the toroids ranges between 2.0 and 6.0 T m across most of the detector. A set of precision chambers covers the region $|\eta| < 2.7$ with three layers of monitored drift tubes, complemented by cathode-strip chambers in the forward region, where the background is highest. The muon trigger system covers the range $|\eta| < 2.4$ with resistive-plate chambers in the barrel, and thin-gap chambers in the endcap regions. Interesting events are selected to be recorded by the first-level trigger system implemented in custom hardware, followed by selections made by algorithms implemented in software in the high-level trigger [46].

² ATLAS uses a right-handed coordinate system with its origin at the nominal interaction point (IP) in the centre of the detector and the z -axis along the beam pipe. The x -axis points from the IP to the centre of the LHC ring, and the y -axis points upwards. Cylindrical coordinates (r, ϕ) are used in the transverse plane, ϕ being the azimuthal angle around the z -axis. The pseudorapidity is defined in terms of the polar angle θ as $\eta = -\ln \tan(\theta/2)$. Angular distance is measured in units of $\Delta R \equiv \sqrt{(\Delta\eta)^2 + (\Delta\phi)^2}$.

The first-level trigger reduces the rate of accepted events from the 40 MHz bunch crossing rate to below 100 kHz, which the high-level trigger further reduces in order to record events to disk at about 1 kHz.

3 Data and simulated event samples

The data used in this analysis were collected by the ATLAS detector during pp collisions at a centre-of-mass energy of $\sqrt{s} = 13$ TeV from 2015 to 2018. The average number $\langle\mu\rangle$ of pp interactions per bunch crossing (pile-up) varies from 14 during 2015 to 38 during 2017-2018. Only events taken in stable beam conditions, and for which all relevant detector systems were operational, are considered in this analysis. After data-quality requirements the data sample amounts to a total integrated luminosity of 139 fb^{-1} . The uncertainty in the combined 2015-2018 integrated luminosity is 1.7% [47], obtained using the LUCID-2 detector [48].

For the two-body and three-body selections, events are selected by a trigger that requires a minimum of two electrons, two muons or an electron and a muon [46]. Different trigger-level thresholds for the transverse momentum of the leptons were used in different data-taking periods, ranging between 8 and 22 GeV. Tighter thresholds are applied in the lepton offline selection, to assure the trigger efficiency is "on plateau" in all the relevant kinematic region. Missing transverse momentum triggers are used in the four-body selection [49] to increase the acceptance of low p_T leptons. The missing transverse momentum trigger threshold varied depending on data taking conditions along the years: 70 GeV for data collected during 2015; in the range 90–110 GeV for data collected during 2016, and 110 GeV for data collected during 2017 and 2018. Tighter offline requirements on the missing transverse momentum are defined accordingly to ensure event selection on the plateau region of the trigger efficiency curve.

Simulated event samples are used for SM background estimations and to model the signal samples. Standard Model MC samples are processed through a full GEANT 4 [50] simulation of the ATLAS detector, while a fast simulation based on parameterisation of the calorimeter response and GEANT 4 simulation for all the other detector components [51] is used for the SUSY and DM signal samples. MC events are reconstructed using the same algorithms used for the data. To compensate for small residual differences between data and simulation in the lepton reconstruction efficiency, energy scale, energy resolution, trigger modelling, and b -tagging efficiency, the simulated events are re-weighted using correction factors derived from data [52–54].

The events targeted by this analysis are characterised by two leptons with opposite electric charge, jets and missing transverse momentum. The main SM background contributions are expected to come from top quark pair production ($t\bar{t}$), associated production of a Z boson with top quark pair ($t\bar{t}Z$), single-top decay via Wt channel (Wt), $Z/\gamma^* + \text{jets}$ and diboson processes (VV with $V = W, Z$).

Matrix element and showering generators used for the SM backgrounds and signals are listed in the Table 1 along with the relevant sets of parton distribution function (PDF), the configuration of underlying-event and hadronisation parameters (tunes), and the cross-section order in α_s used to normalise the event yields. Additional MC samples are used to estimate systematic uncertainties, as detailed in Section 7.

The SUSY top squark pair signal samples were generated from leading-order (LO) matrix elements with up to two extra partons using MADGRAPH5_AMC@NLO 2.6.2 [55]. MADGRAPH5_AMC@NLO was interfaced to PYTHIA 8.212 +MADSPIN [56, 57] for the signal samples used in the three-body and four-body selections, while it was interfaced to PYTHIA 8.212 for the SUSY signal samples used for the interpretation of the two-body selection results. Signal cross-sections were calculated to next-to-leading

order (NLO) in α_s adding the resummation of soft gluon emission at next-to-leading-logarithm accuracy (NLO+NLL) [58–64]. The nominal cross-sections and their uncertainties were taken from an envelope of cross-section predictions using different PDF sets and factorisation and renormalisation scales, as described in Ref. [65]. Jet-parton matching was performed following the CKKW-L prescription [66]. The A14 tune [67] was used for the modelling of the parton showering, hadronisation and the description of the underlying event. Parton luminosities were provided by the NNPDF2.3LO PDF set [68].

The dark matter signal samples were also generated from leading-order matrix elements, with up to one extra parton, using MADGRAPH5_AMC@NLO 2.6.2 interfaced to PYTHIA 8.212 [69]. In the DM samples generation the couplings of the scalar and pseudo-scalar mediator to the DM and SM particles (g_q and g_χ) are set to one. The kinematics of the mediator decay is not strongly dependent on the values of the couplings, however the particle kinematic distributions are sensitive to the nature of the mediator and to the mediator and DM particle masses. The cross-sections were computed at NLO [70, 71].

Inelastic pp interactions were generated and overlaid onto the hard-scattering process to simulate the effect of multiple proton-proton interactions occurring during the same (in-time) or a nearby (out-of-time) bunch crossing. These were produced using PYTHIA 8.186 [56] and EvtGen [72] with the NNPDF2.3LO set of PDFs [68] and the A3 tune [73]. The MC samples were reweighted so that the distribution of the average number of interactions per bunch crossing reproduces the observed distribution in the data.

Table 1: Simulated signal and background event samples with the corresponding matrix element and parton shower (PS) generators, cross-section order in α_s used to normalise the event yield, and the generator and PS PDF sets used.

| Physics process | Generator | Parton shower | Normalisation | PDF (generator) | PDF (PS) |
|--|-------------------------------|--------------------------------|------------------|-------------------|-------------------|
| SUSY Signals (three-body, four-body) | MADGRAPH5_AMC@NLO 2.6.2 [55] | PYTHIA 8.212 +MadSPIN [56, 57] | NLO+NLL [58–64] | NNPDF3.0NLO | NNPDF2.3LO [68] |
| DM, SUSY Signals (two-body) | MADGRAPH5_AMC@NLO 2.6.2 | PYTHIA 8.212 | NLO+NLL | NNPDF3.0NLO | NNPDF2.3LO |
| $t\bar{t}$ | POWHEG-Box v2 [74–76] | PYTHIA 8.230 [69] | NNLO+NNLL [77] | NNPDF3.0NLO [78] | NNPDF2.3LO [68] |
| $t\bar{t} + V(V = W, Z)$ | MADGRAPH5_AMC@NLO [55] | PYTHIA 8.210 [69] | NLO [55, 79] | NNPDF3.0NLO | NNPDF2.3LO |
| $t\bar{t}H$ | POWHEG-Box v2 [74, 75, 80] | PYTHIA 8.230 | NLO [55, 79] | NNPDF3.0NLO | NNPDF2.3LO |
| $t\bar{t}WW$ | MADGRAPH5_AMC@NLO | PYTHIA 8.186 [56] | NLO [55] | NNPDF2.3LO | NNPDF2.3LO |
| $t\bar{t}WZ$ | MADGRAPH5_AMC@NLO | PYTHIA 8.212 [69] | NLO [55] | NNPDF3.0NLO | NNPDF2.3LO |
| $tZ, t\bar{t}t, t\bar{t}t$ | MADGRAPH5_AMC@NLO | PYTHIA 8.230 | NLO [55] | NNPDF3.0NLO | NNPDF2.3LO |
| Single top | POWHEG-Box v2 [74–76, 81, 82] | PYTHIA 8.230 | NLO+NNLL [83–87] | NNPDF3.0NLO | NNPDF2.3LO |
| $Z/\gamma^*(\rightarrow ll) + \text{jets}$ | SHERPA 2.2.1 [88, 89] | SHERPA | NNLO [90] | NNPDF3.0NNLO [78] | NNPDF3.0NNLO [78] |
| Diboson $VV (V = W, Z)$ | SHERPA 2.2.1 or 2.2.2 [88] | SHERPA | NLO [91] | NNPDF3.0NNLO | NNPDF3.0NNLO |
| Triboson $VVV (V = W, Z)$ | SHERPA 2.2.2 [88] | SHERPA | NLO [88, 91] | NNPDF3.0NNLO | NNPDF3.0NNLO |

4 Object identification

Candidate events are required to have a reconstructed vertex with at least two associated tracks with a p_T larger than 500 MeV which originate from the beam collision region in the x - y plane. The primary vertex in the event is the vertex with the highest scalar sum of the squared transverse momentum of associated tracks.

The leptons selected for analysis are classified as baseline and as signal leptons depending on an increasingly stringent set of reconstruction quality criteria and kinematic selections. Baseline objects are used in the calculation of missing transverse momentum ($\mathbf{p}_T^{\text{miss}}$), to resolve ambiguities between the analysis objects in the event, as described later, and for the fake/non-prompt (FNP) lepton background estimation described in Section 6. Signal leptons are used for the final event selection.

Baseline electron candidates are reconstructed from three-dimensional clusters of energy deposition in the electromagnetic calorimeter matched to ID tracks. These electron candidates are required to

have pseudorapidity $|\eta| < 2.47$, $E_T > 4.5$ GeV, and to pass a *Loose* likelihood-based identification requirement [52] with additional condition on the number of hits in the *B*-layer. The tracks associated with electron candidates are required to have a longitudinal impact parameter³ relative to the primary vertex $|z_0 \sin \theta| < 0.5$ mm.

Baseline muon candidates are reconstructed matching ID tracks, in the pseudorapidity region $|\eta| < 2.4$ for the two-body and three-body selection and $|\eta| < 2.7$ for the four-body selection, with MS tracks, or energy deposits in the calorimeter compatible with minimum ionising particle (calo-tagged muon). Associated tracks are required to have a $p_T > 4$ GeV and a $|z_0 \sin \theta| < 0.5$ mm from the primary vertex. Muon candidates are required to satisfy the *Medium* identification requirement, defined in Ref. [53], based on the number of hits in the different ID and MS subsystems, and on the significance of the charge-to-momentum ratio q/p .

Additional tighter selections are applied to the baseline lepton candidates, which are referred as signal electrons or muons. Signal electrons are required to satisfy a *Medium* likelihood-based identification requirement [52] and the track associated with the signal electron is required to have a significance $|d_0|/\sigma(d_0) < 5$, where d_0 is the transverse impact parameter relative to the reconstructed primary vertex and $\sigma(d_0)$ is its uncertainty. Isolation criteria are applied to electrons by placing an upper limit on the sum of the transverse energy of the calorimeter energy clusters in a cone of $\Delta R_\eta = \sqrt{(\Delta\eta)^2 + (\Delta\phi)^2} = 0.2$ around the electron (excluding the deposit from the electron itself) and the scalar sum of the p_T of tracks within a cone $\Delta R_\eta = 0.2$ around the electron (excluding its own track). The isolation criteria are optimised such that the isolation selection efficiency is uniform across η . This varies from 90% for $p_T = 25$ GeV to 99% for $p_T = 60$ GeV in events with a *Z* boson decaying to pair of electrons or muons [52].

For signal muons a significance in the transverse impact parameter $|d_0|/\sigma(d_0) < 3$ is required. Isolation criteria applied to muons require the scalar sum of the p_T of tracks inside a cone with $\Delta R_\eta = 0.3$ around the muon (excluding its own track) to be less than 15% of the muon p_T . In addition, the sum of the transverse energy of the calorimeter energy clusters in a cone of $\Delta R_\eta = 0.2$ around the muon (excluding the energy from the lepton itself) must be less than 30% of the muon p_T [53].

Jets are reconstructed from three-dimensional clusters of energy in the calorimeter [92] using the anti- k_t jet clustering algorithm [93] as implemented in the FastJet package [94], with a radius parameter $R = 0.4$. The reconstructed jets are then calibrated by the application of a jet energy scale derived from 13 TeV data and simulation [95]. Only jet candidates with $p_T > 20$ GeV and $|\eta| < 2.8$ are considered⁴.

To reduce the effects of pile-up, for jets with $|\eta| \leq 2.5$ and $p_T < 120$ GeV a significant fraction of the tracks associated with each jet are required to have an origin compatible with the primary vertex, as defined by the jet vertex tagger (JVT) [96]. This requirement reduces the fraction of jets from pile-up to 1%, with an efficiency for pure hard-scatter jets of about 90%. Finally, in order to remove events impacted by detector noise and non-collision backgrounds, specific jet-quality requirements [97, 98] are applied, designed to provide an efficiency of selecting jets from proton-proton collisions above 99.5% (99.9%) for $p_T > 20$ (100) GeV.

The MV2C10 boosted decision tree algorithm [54] identifies jets containing *b*-hadrons (*‘b-jets’*) by using quantities such as the impact parameters of associated tracks, and well-reconstructed secondary vertices. A

³ The transverse impact parameter is defined as the distance of closest approach in the transverse plane between a track and the beam-line. The longitudinal impact parameter corresponds to the z-coordinate distance between the point along the track at which the transverse impact parameter is defined and the primary vertex.

⁴ Hadronic τ -lepton decay products are treated as jets.

selection that provides 77% efficiency for tagging b -jets in simulated $t\bar{t}$ events is used. The corresponding rejection factors against jets originating from c -quarks, from τ -leptons, and from light quarks and gluons in the same sample at this working point are 4.9, 15 and 110, respectively.

To avoid reconstruction ambiguities and double counting of analysis objects, an overlap removal procedure is applied to the baseline leptons and jets. The calo-tagged muons are removed if sharing the track with electrons. Furthermore, all electrons sharing an ID track with a muon are removed. Jets which are not b -tagged (with the tagging parameters corresponding to an efficiency of 85%) and lying within a cone $\Delta R = \sqrt{\Delta y^2 + \Delta \phi^2} = 0.2$ around an electron candidate are removed. All jets lying within $\Delta R = 0.2$ from an electron are removed if the electron has $p_T > 100$ GeV. Finally any lepton candidate is removed in favour of a jet candidate if it lies within $\Delta R < \min(0.4, 0.04 + 10/p_T(\ell))$ from the jet, where $p_T(\ell)$ is the p_T of the lepton.

The missing transverse momentum, with magnitude E_T^{miss} , is defined as the negative vector sum of the transverse momenta for all baseline electrons, photons, muons and jets. Low-momentum tracks from the primary vertex that are not associated with reconstructed analysis objects are also included in the calculation. The E_T^{miss} value is adjusted for the calibration of the selected physics objects [99]. Linked to the E_T^{miss} value is the "object-based E_T^{miss} significance" called simply E_T^{miss} significance in this paper. This quantity measures the significance of E_T^{miss} based upon the transverse momentum resolution of all objects used in the calculation of the $\mathbf{p}_T^{\text{miss}}$. It is defined as

$$E_T^{\text{miss}} \text{ significance} = \frac{|\mathbf{p}_T^{\text{miss}}|}{\sqrt{\sigma_L^2(1 - \rho_{LT}^2)}}$$

where σ_L (Longitudinal) is the component parallel to the $\mathbf{p}_T^{\text{miss}}$ of the total transverse momentum resolution for all objects in the event and the quantity ρ_{LT} is the correlation factor between the parallel and perpendicular components of the transverse momentum resolution for each object. On an event-by-event basis, given the full event composition, E_T^{miss} significance evaluates the p -value that the observed E_T^{miss} is consistent with the null hypothesis of zero real E_T^{miss} , as further detailed in Ref. [24]. In this way E_T^{miss} significance helps to separate events with true E_T^{miss} , arising from weakly interacting particles such as for example Dark Matter or neutralinos, from those where E_T^{miss} is consistent with particle mismeasurement, resolution or identification inefficiencies thus providing a better background rejection.

5 Event selection

Different event selections are inspired by previous published strategies [22, 23] re-optimised to fully exploit the larger available dataset. For all selections, an improvement in the sensitivity is obtained with the introduction of the E_T^{miss} significance variable, which enables further optimisation on the selection variables. The four-body sensitivity also benefits from a reduction in the lepton p_T threshold in the region with small mass differences $\Delta m(\tilde{t}_1, \tilde{\chi}_1^0)$ between \tilde{t}_1 and $\tilde{\chi}_1^0$. The threshold for the muon (electron) p_T has been lowered from 7 GeV to 4 GeV (4.5 GeV).

Events are required to have exactly two signal leptons (electrons, muons, or one of each) with opposite electric charge. In the two-body and three-body selections, an invariant mass $m_{\ell\ell}$ greater than 20 GeV is applied to remove leptons from Drell-Yan and low-mass resonances while in the four-body selection, given the softer p_T spectrum of the leptons, $m_{\ell\ell}$ is required to be higher than 10 GeV. Events with same

flavour (SF) lepton pairs ($e^\pm e^\mp$ and $\mu^\pm \mu^\mp$) with $m_{\ell\ell}$ between 71.2 and 111.2 GeV are rejected to reduce the Z boson background, except for the four-body selection. No additional $m_{\ell\ell}$ selection is applied on the different flavour (DF) lepton pairs ($e^\pm \mu^\mp$). Different jet (b -jet) multiplicities, labeled as n_{jets} ($n_{b\text{-jets}}$), are required in the three selections, as detailed below.

5.1 Discriminators and kinematic variables

Final event selections are obtained by maximizing the separation between signal and SM background using different kinematic variables. Two variables are constructed from the E_T^{miss} and the p_T of the leading leptons and jets:

$$R_{2\ell} = E_T^{\text{miss}} / (p_T(\ell_1) + p_T(\ell_2)) \quad \text{and} \quad R_{2\ell 4j} = E_T^{\text{miss}} / \left(E_T^{\text{miss}} + p_T(\ell_1) + p_T(\ell_2) + \sum_{i=1, \dots, N \leq 4} p_T(j_i) \right)$$

where $p_T(\ell_1)$ and $p_T(\ell_2)$ are the leading and subleading lepton transverse momenta and $p_T(j_{i=1, \dots, N \leq 4})$ are the transverse momenta of the four leading jets, in decreasing order. For some backgrounds, e.g. $Z/\gamma^* + \text{jets}$, the variable $R_{2\ell}$ has a distribution with a peak at lower values with respect to the signal, and it is thus used to reject them. Similarly, $R_{2\ell 4j}$ is employed for its high rejection power against multi-jet events.

Another variable employed is $\mathbf{p}_{T, \text{boost}}^{\ell\ell}$ which is defined as the vectorial sum of $\mathbf{p}_T^{\text{miss}}$ and the leptons transverse momentum vectors $\mathbf{p}_T(\ell_1)$ and $\mathbf{p}_T(\ell_2)$. Its magnitude, $p_{T, \text{boost}}^{\ell\ell}$, can be interpreted as the opposite of the vector sum of all the transverse hadronic activity in the event. The azimuthal angle between the $\mathbf{p}_T^{\text{miss}}$ vector and the $\mathbf{p}_{T, \text{boost}}^{\ell\ell}$ vector is defined as $\Delta\phi_{\text{boost}}$. This variable is useful to select events where the leptonic component (e , μ and neutrinos) is collimated.

The lepton-based transverse mass [100, 101] is a kinematic variable used to bound the masses of a pair of identical particles which have each decayed into a visible and an invisible particle. This quantity is defined as

$$m_{T2}(\mathbf{p}_{T,1}, \mathbf{p}_{T,2}, \mathbf{p}_T^{\text{miss}}) = \min_{\mathbf{q}_{T,1} + \mathbf{q}_{T,2} = \mathbf{p}_T^{\text{miss}}} \left\{ \max[m_T(\mathbf{p}_{T,1}, \mathbf{q}_{T,1}), m_T(\mathbf{p}_{T,2}, \mathbf{q}_{T,2})] \right\},$$

where m_T indicates the transverse mass,⁵ $\mathbf{p}_{T,1}$ and $\mathbf{p}_{T,2}$ are the transverse momentum vectors of two visible particles, and $\mathbf{q}_{T,1}$ and $\mathbf{q}_{T,2}$ are transverse momentum vectors with $\mathbf{p}_T^{\text{miss}} = \mathbf{q}_{T,1} + \mathbf{q}_{T,2}$. The minimisation is performed over all the possible decompositions of $\mathbf{p}_T^{\text{miss}}$. In this paper, $\mathbf{p}_{T,1}$ and $\mathbf{p}_{T,2}$ are the transverse momentum vectors of the two leptons and $m_{T2}(\mathbf{p}_T(\ell_1), \mathbf{p}_T(\ell_2), \mathbf{p}_T^{\text{miss}})$ is referred to simply as $m_{T2}^{\ell\ell}$. The $m_{T2}^{\ell\ell}$ distribution is expected to have an endpoint corresponding to the W mass for backgrounds such as $t\bar{t}$ while it is expected to reach higher values in case of SUSY events, due to the presence of the neutralinos [102, 103].

The three-body selection uses a number of ‘super-razor’ variables [104], which are derived under a series of assumptions made in order to approximate the center-of-mass energy frame (Razor Frame) of two parent particles (i.e. top squarks) and the decay frames. Each parent particle is assumed to decay into a set of visible (only leptons are considered in this case) and invisible particles (i.e. neutrinos and neutralinos). These variables are R_{p_T} , the Lorentz factor γ_{R+1} , the azimuthal angle $\Delta\phi_\beta^R$ and M_Δ^R . The first variable is $R_{p_T} = |\vec{J}_T| / (|\vec{J}_T| + \sqrt{s_R}/4)$ with \vec{J}_T as the vector sum of the transverse momenta of the visible particles and

⁵ The transverse mass is defined by the equation $m_T(\mathbf{p}_T, \mathbf{q}_T) = \sqrt{2|\mathbf{p}_T||\mathbf{q}_T|(1 - \cos(\Delta\phi))}$, where $\Delta\phi$ is the angle between particles of negligible mass with transverse momenta \mathbf{p}_T and \mathbf{q}_T .

the missing transverse momentum, and $\sqrt{\hat{s}_R}$ as an estimate of the system's energy in the razor frame R , defined as the frame in which the two visible leptons have equal and opposite longitudinal momentum (p_z). $|\vec{J}_T|$ vanishes for events where leptons are the only visible particles, such as diboson events, leading to R_{pT} values that tend toward zero. Instead, in events that contain additional activity, such as $t\bar{t}$, this variable tends towards unity. The Lorentz factor, γ_{R+1} , is instead associated with the boost from the razor frame R to the approximation of the two decay frames of the parent particles and is expected to have values tending towards unity for back-to-back visible particles or when they have different momentum. Lower values of γ_{R+1} are otherwise expected when the two visible particles are collinear and with comparable momentum. The azimuthal angle $\Delta\phi_\beta^R$ is defined between the razor boost from the laboratory to the R frame and the sum of the visible momenta as evaluated in the R frame. It is a good discriminator to be used in searches for models with small mass differences between the massive pair-produced particle and the invisible particle produced in the decay. Finally, the last variable is $M_\Delta^R = \sqrt{\hat{s}_R}/\gamma_{R+1}$ which is particularly powerful in the discrimination of the signal events against $t\bar{t}$ and diboson background rejection, since it has a kinematic end-point that is proportional to the mass-splitting between the parent particle and the invisible particle.

5.2 Two-body event selection

This selection targets the dark matter signal model that assumes the production of a pair of dark matter particles through the exchange of a spin-0 mediator, in association with a pair of top quarks (Figure 1(c)).

For each event, the leading lepton, ℓ_1 , is required to have $p_T(\ell_1) > 25$ GeV, while for the sub-leading lepton, ℓ_2 , the requirement is $p_T(\ell_2) > 20$ GeV. Events are further selected with at least one reconstructed b -jet, $\Delta\phi_{\text{boost}}$ lower than 1.5 and E_T^{miss} significance greater than 12, and finally with $m_{T2}^{\ell\ell}$ greater than 110 GeV. Following the classification of the events, two sets of signal regions (SRs) are defined: a set of exclusive SRs *binned* in the $m_{T2}^{\ell\ell}$ variable, to maximise model-dependent search sensitivity, and a set of *inclusive* SRs, to be used for model-independent results. For the binned SRs, events are separated accordingly to the lepton flavours, different flavour or same flavour, and by the range $[x, y)$ of the $m_{T2}^{\ell\ell}$ interval: SR-DF $_{x,y}^{2\text{-body}}$ or SR-SF $_{x,y}^{2\text{-body}}$. For the inclusive signal regions, referred to as SR $_{x,\infty}^{2\text{-body}}$ with x being the lower limit applied to the $m_{T2}^{\ell\ell}$ variable, DF and SF events are combined. The common definition of these two sets of signal regions is shown in Table 2.

Table 2: *Two-body selection*. Common definition of the binned and the inclusive sets of signal regions.

| | SR $^{2\text{-body}}$ |
|-----------------------------------|-----------------------|
| Leptons flavour | DF SF |
| $p_T(\ell_1)$ [GeV] | > 25 |
| $p_T(\ell_2)$ [GeV] | > 20 |
| $m_{\ell\ell}$ [GeV] | > 20 |
| $ m_{\ell\ell} - m_Z $ [GeV] | – > 20 |
| $n_{b\text{-jets}}$ | ≥ 1 |
| $\Delta\phi_{\text{boost}}$ [rad] | < 1.5 |
| E_T^{miss} significance | > 12 |
| $m_{T2}^{\ell\ell}$ [GeV] | > 110 |

5.3 Three-body event selection

The three-body decay mode of the top squark shown in Figure 1(a) is dominant in the region where $m(\tilde{t}_1) > m(\tilde{\chi}_1^0) + m(W) + m(b)$ and $m(\tilde{t}_1) < m(\tilde{\chi}_1^0) + m(t)$. The signal kinematics in this region resemble that of WW production when $\Delta m(\tilde{t}, \tilde{\chi}_1^0) \sim m(W)$ and that of $t\bar{t}$ when $\Delta m(\tilde{t}, \tilde{\chi}_1^0) \sim m(t)$. The signal selection has been optimised to reject these dominant backgrounds while not degrading signal efficiency. The b -jet multiplicity is highly dependent on the mass splitting between the top squark and the neutralino, $\Delta m(\tilde{t}_1, \tilde{\chi}_1^0) = m(\tilde{t}_1) - m(\tilde{\chi}_1^0)$, since for lower $\Delta m(\tilde{t}_1, \tilde{\chi}_1^0)$ the b -jets have lower momentum and cannot be reconstructed efficiently. Accordingly, two orthogonal signal regions have been defined: $\text{SR}_W^{3\text{-body}}$ targeting $\Delta m(\tilde{t}, \tilde{\chi}_1^0) \sim m(W)$, applying a b -jet veto, and $\text{SR}_t^{3\text{-body}}$ targeting $\Delta m(\tilde{t}, \tilde{\chi}_1^0) \sim m(t)$, allowing for b -jets. Separation between same flavour and different flavour events is also kept to optimise model-dependent search sensitivity, thus defining four different SRs: $\text{SR-DF}_W^{3\text{-body}}$, $\text{SR-SF}_W^{3\text{-body}}$, $\text{SR-DF}_t^{3\text{-body}}$ and $\text{SR-SF}_t^{3\text{-body}}$. The signal regions make use of a common set of requirements on the p_T of the two leptons, E_T^{miss} significance and γ_{R+1} . The definitions of these regions are summarised in Table 3.

Table 3: *Three-body selection.* Signal regions definition.

| | $\text{SR}_W^{3\text{-body}}$ | | $\text{SR}_t^{3\text{-body}}$ | |
|----------------------------------|-------------------------------|--------|-------------------------------|--------|
| Leptons flavour | DF | SF | DF | SF |
| $p_T(\ell_1)$ [GeV] | > 25 | | > 25 | |
| $p_T(\ell_2)$ [GeV] | > 20 | | > 20 | |
| $m_{\ell\ell}$ [GeV] | > 20 | | > 20 | |
| $ m_{\ell\ell} - m_Z $ [GeV] | – | > 20 | – | > 20 |
| $n_{b\text{-jets}}$ | $= 0$ | | ≥ 1 | |
| $\Delta\phi_\beta^R$ [rad] | > 2.3 | | > 2.3 | |
| E_T^{miss} significance | > 12 | | > 12 | |
| $1/\gamma_{R+1}$ | > 0.7 | | > 0.7 | |
| R_{p_T} | > 0.78 | | > 0.70 | |
| M_Δ^R [GeV] | > 105 | | > 120 | |

5.4 Four-body event selection

In the kinematic region defined by $m(\tilde{t}_1) < m(\tilde{\chi}_1^0) + m(b) + m(W)$ and $m(\tilde{t}_1) > m(\tilde{\chi}_1^0) + m(b)$, the top squarks are assumed to decay via a four-body process through an off-shell top quark and W boson as shown in Figure 1(b). In this region the final state leptons from the virtual W boson decay are expected to have lower momentum and can be efficiently selected when imposing both a lower and upper bound on the p_T of the leptons. A lower transverse momentum threshold of 4.5 GeV (4 GeV) is applied for electrons (muons), together with an upper threshold, which is optimised separately for the leading and the sub-leading leptons. Two separate signal regions are defined to cover effectively the different $\Delta m(\tilde{t}_1, \tilde{\chi}_1^0)$: the first one, $\text{SR}_{\text{Small } \Delta m}^{4\text{-body}}$, targets small values of $\Delta m(\tilde{t}_1, \tilde{\chi}_1^0)$ and requires $p_T(\ell_1) < 25$ GeV and $p_T(\ell_2) < 10$ GeV; the second one, $\text{SR}_{\text{Large } \Delta m}^{4\text{-body}}$, targets larger values of $\Delta m(\tilde{t}_1, \tilde{\chi}_1^0)$ and instead requires $p_T(\ell_2) > 10$ GeV. This

condition assures also the orthogonality between the two SRs. The presence of an energetic initial state radiation (ISR) jet recoiling against the system of the two top squarks is required, introducing an unbalance in the event kinematics with an enhanced value of E_T^{miss} that allows signal events to be distinguished from SM processes. For this reason, for each event, the leading jet j_1 is considered to be a jet from ISR and required to have $p_T > 150$ GeV. A further reduction of the SM background is achieved with selections on E_T^{miss} significance, $p_{T,\text{boost}}^{\ell\ell}$, $R_{2\ell}$ and $R_{2\ell 4j}$ variables. An additional requirement is applied to improve the sub-leading lepton isolation, using the following isolation variable:

$$\min \Delta R_{\ell_2, j_i} = \min_{j_i \in [\text{jets}]} \Delta R_{\eta}(l_2, j_i)$$

where ‘[jets]’ contains all the jets in the event. This reduces the probability of lepton misidentification or selecting a lepton originating from heavy flavour or π/K decays in jets. The definition of these regions are summarised in Table 4.

Table 4: *Four-body selection. Signal regions definition.*

| | SR ^{4-body} _{Small Δm} | SR ^{4-body} _{Large Δm} |
|---------------------------------------|---|---|
| $p_T(\ell_1)$ [GeV] | [4.5(4), 25] $e(\mu)$ | < 100 |
| $p_T(\ell_2)$ [GeV] | [4.5(4), 10] $e(\mu)$ | [10, 50] |
| $m_{\ell\ell}$ [GeV] | > 10 | |
| $p_T(j_1)$ [GeV] | > 150 | |
| $\min \Delta R_{\ell_2, j_i}$ | > 1 | |
| E_T^{miss} significance | > 10 | |
| $p_{T,\text{boost}}^{\ell\ell}$ [GeV] | > 280 | |
| E_T^{miss} [GeV] | > 400 | |
| $R_{2\ell}$ | > 25 | > 13 |
| $R_{2\ell 4j}$ | > 0.44 | > 0.38 |

6 Background estimation

The MC predictions for the dominant SM background processes are corrected using a data driven normalisation procedure, while non-dominant processes are estimated directly using MC. A simultaneous profile likelihood fit [105] is used to constrain the MC yields with the observed data in dedicated background control regions (CRs). The fit is performed using standard minimisation software [106, 107] where the normalisations of the targeted backgrounds are allowed to float, while the MC simulation is used to describe the shape of kinematical variables. Systematic uncertainties that could affect the expected yields in the different regions are taken into account in the fit through nuisance parameters. Each uncertainty source is described by a single nuisance parameter, and correlations between nuisance parameters, background processes and selections are taken into account. The list of systematic uncertainties considered in the fits is provided in Section 7. The SM background thus modelled is verified in dedicated Validation Regions (VRs) which are disjoint from both the control and signal regions.

Important sources of reducible backgrounds come from jets which are misidentified as leptons. The fake/non-prompt (FNP) lepton background comes from π/K and heavy flavour hadron decays and photon

conversions. This is particularly important for the low p_T leptons targeted by the four-body selection. The FNP background is mainly suppressed by the lepton isolation requirements described in Section 4 but a non-negligible residual contribution is expected. This is estimated from data using the ‘fake factor’ method [108–112] which uses two orthogonal lepton definitions, labeled as ‘Id’ and ‘anti-Id’, to define a control data sample enriched in fake leptons. The Id lepton corresponds to the signal lepton identification criteria used in this analysis. Anti-Id electrons fail either the identification or isolation requirement, while anti-Id muons fail the isolation one. The sample used for the fake factor computation is enriched in Z +jets events. Events with three leptons are selected, with the two same flavour opposite electric charge leptons (SFOS) identified as the Z boson decay products (ℓ_1^Z and ℓ_2^Z , in order of decreasing p_T) satisfying the Id requirements, and the third unpaired lepton, called *probe* (ℓ^{probe}), satisfying either the Id or anti-Id criteria. The fake factor is defined as the ratio between the yields of the Id and the anti-Id probe leptons. Residual contributions from processes producing prompt leptons are subtracted using the MC predictions. Fake factors are measured separately for electrons and muons and as a function of the lepton p_T and η . These are derived in the CR^{FNP} region whose selection is summarised in Table 5. The FNP estimates in the various analysis regions are derived applying the fake factors to events satisfying the same regions criteria but replacing at least one of the signal leptons by an anti-Id one.

Table 5: *FNP selection*. Detailed definition of the CR^{FNP} region.

| | CR^{FNP} |
|---|---|
| Lepton multiplicity | 3 |
| $ m_{\ell\ell} - m_Z $ [GeV] | < 10 for SFOS pair |
| $p_T(\ell_1^Z)$ [GeV] | > 25 |
| $p_T(\ell_2^Z)$ [GeV] | > 20 |
| $p_T(\ell^{\text{probe}})$ [GeV] | $> 4.5(4) e(\mu)$ |
| $\Delta R_\eta(\ell^{\text{probe}}, \ell_i)$ | > 0.2 |
| $m_T(\ell^{\text{probe}}, E_T^{\text{miss}})$ [GeV] | < 40 |
| Additional requirements | $p_T(\ell^{\text{probe}}) < 16$ GeV or $E_T^{\text{miss}} < 50$ GeV |

The three selections in this paper use different sets of CRs and VRs, specifically designed to be kinematically similar to the respective SRs. The definitions of the regions used in each analysis and the results of the fits are described in the following subsections.

6.1 Estimation of the backgrounds in the two-body selection

The main background sources for the two-body selection are $t\bar{t}$ and $t\bar{t}Z$ with invisible decay of the Z boson. These processes are normalised to data in dedicated CRs: $\text{CR}_{t\bar{t}}^{2\text{-body}}$ and $\text{CR}_{t\bar{t}Z}$. The $t\bar{t}$ normalisation factor is extracted from different-flavour events. In order to test the reliability of the $t\bar{t}$ background prediction, two validation region $\text{VR-DF}_{t\bar{t}}^{2\text{-body}}$ and $\text{VR-SF}_{t\bar{t}}^{2\text{-body}}$ are defined. The $t\bar{t}Z$ production events with invisible decay of the Z boson are expected to strongly populate the tail of the $m_{T2}^{\ell\ell}$ distribution in the SRs and are normalised in the dedicated control region $\text{CR}_{t\bar{t}Z}$. Given the difficulty in achieving sufficient purity for this SM process due to the high contamination of $t\bar{t}$ events, a strategy based on a three lepton final

state is adopted. Events are selected if characterised by three charged leptons including at least one same flavour and opposite electric charge pair with invariant mass consistent with that of the Z boson ($|m_{\ell\ell} - m_Z| < 20$ GeV). Events are further required to have a jet multiplicity, n_{jets} , greater than two with at least one b -tagged jet. These selections target $t\bar{t}Z$ production with the Z boson decaying to two leptons and $t\bar{t}$ decaying in the semi-leptonic channel. In order to select $t\bar{t}Z$ events whose kinematics, regardless of subsequent $t\bar{t}$ and Z decays, emulate the kinematics of this background in the SRs, the momentum of the two leptons of the SFOS pair ($\mathbf{p}_{\ell_1}^Z, \mathbf{p}_{\ell_2}^Z$) are vectorially added to the $\mathbf{p}_T^{\text{miss}}$, effectively treating them like the neutrino pair from the Z boson decay. A new variable called $E_{T,\text{corr}}^{\text{miss}} = \left| \left(\mathbf{p}_T^{\text{miss}} + \mathbf{p}_{\ell_1}^Z + \mathbf{p}_{\ell_2}^Z \right)_T \right|$ is constructed. Events characterised by high $m_{T2}^{\ell\ell}$ in the SRs are emulated by requiring high $E_{T,\text{corr}}^{\text{miss}}$ values in $\text{CR}_{t\bar{t}Z}$. In order to check the $t\bar{t}Z$ background estimation, the validation region $\text{VR}_{t\bar{t}Z}^{2\text{-body}}$ has been defined. For this region, events with four leptons are selected and required to have at least two SFOS leptons compatible with the Z boson decay. A variant of the m_{T2} variable called $m_{T2}^{4\ell}$ is defined from the $E_{T,\text{corr}}^{\text{miss}}$ and the momentum of the remaining two leptons. The definition of the control and validation regions used in the two-body selection is summarised in Table 6. The expected signal contamination in the CRs is generally below $\sim 1\%$. The signal contamination in the VRs is less than 15% (7%) for a DM signal model with scalar (pseudoscalar) mediator mass of 100 GeV and DM mass of 1 GeV.

Table 6: *Two-body selection.* Control and validation regions definition. The common selection defined in Section 5 also applies to all regions.

| | $\text{CR}_{t\bar{t}}^{2\text{-body}}$ | $\text{CR}_{t\bar{t}Z}$ | $\text{VR-DF}_{t\bar{t}}^{2\text{-body}}$ | $\text{VR-SF}_{t\bar{t}}^{2\text{-body}}$ | $\text{VR}_{t\bar{t}Z}^{2\text{-body}}$ |
|---|--|--|---|---|---|
| Lepton multiplicity | 2 | 3 | 2 | | 4 |
| Lepton flavour | DF | at least one SFOS pair | DF | SF | at least one SFOS pair |
| $p_T(\ell_1)$ [GeV] | > 25 | > 25 | > 25 | | > 25 |
| $p_T(\ell_2)$ [GeV] | > 20 | > 20 | > 20 | | > 20 |
| $p_T(\ell_3)$ [GeV] | – | > 20 | – | | > 20 |
| $p_T(\ell_4)$ [GeV] | – | – | – | | > 20 |
| $m_{\ell\ell}$ | > 20 | – | > 20 | | – |
| $ m_{\ell\ell} - m_Z $ [GeV] | – | < 20 for at least one SFOS pair | – | > 20 | < 20 for at least one SFOS pair |
| $n_{b\text{-jets}}$ | ≥ 1 | ≥ 2 with $n_{\text{jets}} \geq 3$ | ≥ 1 | | > 0 |
| $\Delta\phi_{\text{boost}}$ [rad] | ≥ 1.5 | – | < 1.5 | | – |
| E_T^{miss} significance | > 8 | – | > 12 | | – |
| $E_{T,\text{corr}}^{\text{miss}}$ [GeV] | – | > 140 | – | | – |
| $m_{T2}^{\ell\ell}$ [GeV] | [100, 120] | – | [100, 110] | | – |
| $m_{T2}^{4\ell}$ [GeV] | – | – | – | | > 110 |

Figure 2 illustrates the modelling of the shape of variables after the background fit: (a) shows the $\Delta\phi_{\text{boost}}$ distribution with the $\text{CR}_{t\bar{t}}^{2\text{-body}}$ selection, and (b) shows the $m_{\ell\ell}$ distribution of the SFOS leptons in the $\text{CR}_{t\bar{t}Z}$ selection. Good agreement is found between the data and the background model for all selection variables.

The results of the fit are reported in Table 7 for the two-body CRs and VRs. The normalisations for fitted backgrounds are found to be consistent with the theoretical predictions, when uncertainties are considered: the normalisation factors obtained from the fit for the $t\bar{t}$ and $t\bar{t}Z$ are 0.88 ± 0.08 and 1.07 ± 0.14 respectively. Good agreement, within one standard deviation from the SM background prediction, is observed in the VRs (see Figure 3).

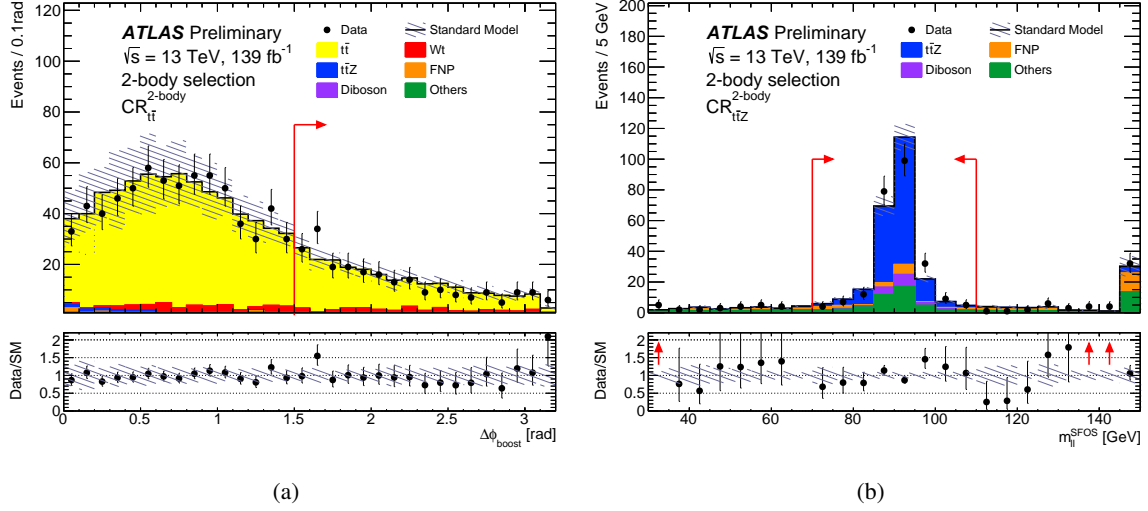


Figure 2: *Two-body selection.* Distributions of (a) $\Delta\phi_{\text{boost}}$ in $\text{CR}_{t\bar{t}}$ (b) $m_{\ell\ell}$ of the two same flavour and opposite sign leptons candidate in $\text{CR}_{t\bar{t}Z}$ after the background fit. The contributions from all SM backgrounds are shown as a histogram stack. "Others" include the contributions from VVV , $t\bar{t}$, $t\bar{t}t$, $t\bar{t}W$, $t\bar{t}WW$, $t\bar{t}WZ$, $t\bar{t}H$, and tZ . The hatched bands represent the total statistical and detector-related systematic uncertainty. The rightmost bin of (b) includes overflow events. In the upper panels red arrows indicate the control region selection criteria. In the bottom panels red arrows show data outside the y-axis range.

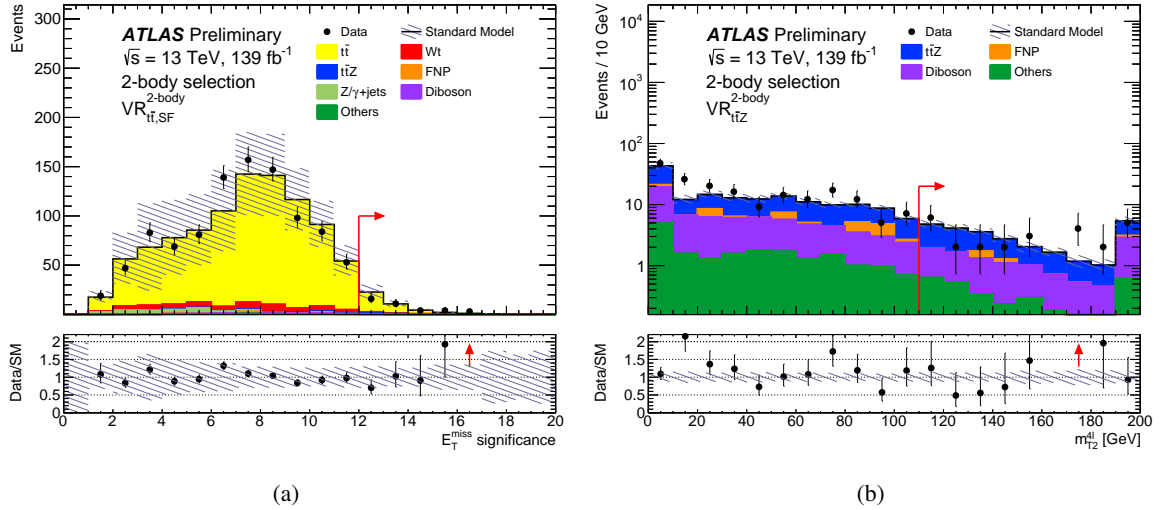


Figure 3: *Two-body selection.* Distributions of the E_T^{miss} significance in (a) $\text{VR-SF}_{t\bar{t}}$ (b) $m_{T2}^{4\ell}$ in $\text{VR}_{t\bar{t}Z}$ after the background fit. The contributions from all SM backgrounds are shown as a histogram stack. "Others" include contributions from VVV , $t\bar{t}$, $t\bar{t}t$, $t\bar{t}W$, $t\bar{t}WW$, $t\bar{t}WZ$, $t\bar{t}H$, and tZ processes. The hatched bands represent the total statistical and detector-related systematic uncertainty. The rightmost bin of each plot includes overflow events. In the upper panels red arrows indicate the validation region selection criteria. In the bottom panels red arrows show data outside the y-axis range.

Table 7: *Two-body selection.* Background fit results for $\text{CR}_{t\bar{t}}^{2\text{-body}}$, $\text{CR}_{t\bar{t}Z}$, $\text{VR-DF}_{t\bar{t}}^{2\text{-body}}$, $\text{VR-SF}_{t\bar{t}}^{2\text{-body}}$ and $\text{VR}_{t\bar{t}Z}^{2\text{-body}}$. "Others" include contributions from VVV , $t\bar{t}t$, $t\bar{t}t\bar{t}$, $t\bar{t}W$, $t\bar{t}WW$, $t\bar{t}WZ$, $t\bar{t}H$, and $t\bar{t}Z$ processes. Combined statistical and systematic uncertainties are given. Entries marked '–' indicate a negligible background contribution.

| | $\text{CR}_{t\bar{t}}^{2\text{-body}}$ | $\text{CR}_{t\bar{t}Z}$ | $\text{VR-DF}_{t\bar{t}}^{2\text{-body}}$ | $\text{VR-SF}_{t\bar{t}}^{2\text{-body}}$ | $\text{VR}_{t\bar{t}Z}^{2\text{-body}}$ |
|----------------------------|--|-------------------------|---|---|---|
| Observed events | 230 | 247 | 45 | 38 | 26 |
| Total (post-fit) SM events | 230 ± 15 | 246 ± 16 | 50 ± 15 | 42 ± 11 | 25.7 ± 3.4 |
| Post-fit, $t\bar{t}$ | 196 ± 17 | – | 44 ± 15 | 36 ± 11 | – |
| Post-fit, $t\bar{t}Z$ | 0.49 ± 0.23 | 170 ± 22 | 1.7 ± 0.6 | 1.9 ± 0.6 | 14.0 ± 2.1 |
| Wt | 31 ± 7 | – | 2.7 ± 1.2 | 2.6 ± 1.2 | – |
| $Z/\gamma^* + \text{jets}$ | – | – | – | – | – |
| Diboson | 1.0 ± 0.6 | 17 ± 4 | 0.50 ± 0.25 | 0.59 ± 0.32 | 8.7 ± 3.0 |
| Others | 1.1 ± 0.5 | 44 ± 12 | 1.0 ± 0.6 | 0.8 ± 0.5 | 3.01 ± 0.87 |
| Fake and non-prompt | $0.0^{+0.5}_{-0.0}$ | 16 ± 8 | $0.0^{+0.5}_{-0.0}$ | $0.0^{+0.5}_{-0.0}$ | $0.0^{+0.5}_{-0.0}$ |

6.2 Estimation of the backgrounds in the three-body selection

The dominant SM backgrounds in the three-body signal regions are diboson, $t\bar{t}$ and $t\bar{t}Z$ productions. Dedicated CRs have been defined, labeled as $\text{CR}_{VV}^{3\text{-body}}$ and $\text{CR}_{t\bar{t}}^{3\text{-body}}$, which are kinematically close to the SRs and which have good purity in diboson and $t\bar{t}$ events respectively. The normalisation of the $t\bar{t}Z$ background is extracted using the same control region $\text{CR}_{t\bar{t}Z}$ defined for the two-body selection in Section 6.1. Dedicated validation regions have been defined to test the modelling of these processes; $\text{VR}_{VV}^{3\text{-body}}$ for the diboson background and $\text{VR}(1)_{t\bar{t}}^{3\text{-body}}$ and $\text{VR}(2)_{t\bar{t}}^{3\text{-body}}$ for the validation of the $t\bar{t}$ background; $\text{VR}(1)_{t\bar{t}}^{3\text{-body}}$ is characterised by a b -jet veto while at least one b -jet is required in $\text{VR}(2)_{t\bar{t}}^{3\text{-body}}$. The definition of the control and validation regions is summarised in Table 8. The expected signal contamination is below 2% in the CRs and below 10% in the VRs for a top squark mass of ~ 430 GeV.

Table 9 shows the expected and observed numbers of events in each of the control and validation regions after the background fit. The normalisation factors extracted from the fit of the backgrounds for the diboson, $t\bar{t}$ and $t\bar{t}Z$ production processes are 0.92 ± 0.28 , 0.96 ± 0.09 and 1.06 ± 0.15 respectively. The total number of fitted background events in the validation regions is in agreement with the observed number of data events. Figure 4 shows the distribution of $\Delta\phi_{\beta}^R$ for the $\text{CR}_{VV}^{3\text{-body}}$ selection and for the $\text{CR}_{t\bar{t}}^{3\text{-body}}$ after the background fit, illustrating the MC modelling of the shape for this variable. Figure 5 shows distributions of R_{pT} in $\text{VR}(1)_{t\bar{t}}^{3\text{-body}}$ and $\text{VR}(2)_{t\bar{t}}^{3\text{-body}}$, and of $\Delta\phi_{\beta}^R$ in $\text{VR}_{VV}^{3\text{-body}}$, after the background fit. Good agreement, within one standard deviation from the SM background prediction, is observed in the validation regions.

Table 8: *Three-body selection*. Control and validation regions definitions. The common selection defined in Section 5 also applies to all regions. Control region $\text{CR}_{t\bar{t}Z}$ is defined in Table 7.

| | $\text{CR}_{t\bar{t}}^{3\text{-body}}$ | $\text{CR}_{VV}^{3\text{-body}}$ | $\text{VR}(1)_{t\bar{t}}^{3\text{-body}}$ | $\text{VR}(2)_{t\bar{t}}^{3\text{-body}}$ | $\text{VR}_{VV}^{3\text{-body}}$ |
|----------------------------------|--|----------------------------------|---|---|----------------------------------|
| Lepton flavour | DF | DF+SF | DF | DF | DF+SF |
| $p_T(\ell_1)$ [GeV] | > 25 | > 25 | > 25 | > 25 | > 25 |
| $p_T(\ell_2)$ [GeV] | > 20 | > 20 | > 20 | > 20 | > 20 |
| $m_{\ell\ell}$ [GeV] | > 20 | > 20 | > 20 | > 20 | > 20 |
| $ m_{\ell\ell} - m_Z $ [GeV] | – | > 20 (SF only) | – | – | > 20 (SF only) |
| $n_{b\text{-jets}}$ | ≥ 2 | $= 0$ | $= 0$ | ≥ 1 | $= 0$ |
| M_{Δ}^R [GeV] | > 80 | > 100 | [80, 105] | [80, 120] | > 100 |
| R_{p_T} | – | > 0.3 | > 0.7 | > 0.7 | > 0.7 |
| $1/\gamma_{R+1}$ | > 0.7 | > 0.7 | > 0.7 | > 0.7 | [0.45, 0.7] |
| E_T^{miss} significance | > 10 | > 10 | > 12 | > 12 | > 12 |
| $\Delta\phi_{\beta}^R$ [rad] | < 2.3 | < 2.3 | > 2.3 | > 2.3 | > 2.3 |

Table 9: *Three-body selection*. Background fit results for $\text{CR}_{VV}^{3\text{-body}}$, $\text{CR}_{t\bar{t}}^{3\text{-body}}$, $\text{CR}_{t\bar{t}Z}$, $\text{VR}_{VV}^{3\text{-body}}$, $\text{VR}(1)_{t\bar{t}}^{3\text{-body}}$ and $\text{VR}(2)_{t\bar{t}}^{3\text{-body}}$. "Others" include contributions from VVV , $t\bar{t}$, $t\bar{t}t\bar{t}$, $t\bar{t}W$, $t\bar{t}WW$, $t\bar{t}WZ$, $t\bar{t}H$, and tZ processes. Combined statistical and systematic uncertainties are given. Entries marked '–' indicate a negligible background contribution.

| | $\text{CR}_{t\bar{t}}^{3\text{-body}}$ | $\text{CR}_{VV}^{3\text{-body}}$ | $\text{CR}_{t\bar{t}Z}$ | $\text{VR}(1)_{t\bar{t}}^{3\text{-body}}$ | $\text{VR}(2)_{t\bar{t}}^{3\text{-body}}$ | $\text{VR}_{VV}^{3\text{-body}}$ |
|----------------------------|--|----------------------------------|-------------------------|---|---|----------------------------------|
| Observed events | 192 | 169 | 247 | 41 | 137 | 84 |
| Total (post-fit) SM events | 192 ± 14 | 169 ± 13 | 247 ± 16 | 38.3 ± 5.9 | 142 ± 25 | 97 ± 15 |
| Post-fit, $t\bar{t}$ | 180 ± 14 | 65 ± 14 | – | 25 ± 5 | 130 ± 24 | 44 ± 11 |
| Post-fit, $t\bar{t}Z$ | 1.57 ± 0.33 | 1.36 ± 0.31 | 172 ± 23 | $0.07^{+0.12}_{-0.07}$ | 1.6 ± 0.7 | 1.0 ± 0.4 |
| Post-fit, diboson | 0.063 ± 0.035 | 74 ± 21 | 16 ± 7 | 11 ± 4 | 0.9 ± 0.5 | 41 ± 14 |
| Wt | 9.0 ± 1.4 | 7.6 ± 2.3 | – | 1.9 ± 0.6 | 8.1 ± 2.0 | 8.1 ± 1.1 |
| $Z/\gamma^* + \text{jets}$ | – | 13 ± 5 | – | – | – | $0.04^{+0.05}_{-0.04}$ |
| Others | 1.39 ± 0.21 | 3.57 ± 0.24 | 43 ± 12 | 0.27 ± 0.06 | 1.11 ± 0.18 | 1.15 ± 0.11 |
| Fake and non-prompt | $0.00^{+0.22}_{-0.00}$ | 5.0 ± 1.9 | 16 ± 8 | $0.00^{+0.27}_{-0.00}$ | $0.00^{+0.27}_{-0.00}$ | 1.8 ± 1.5 |

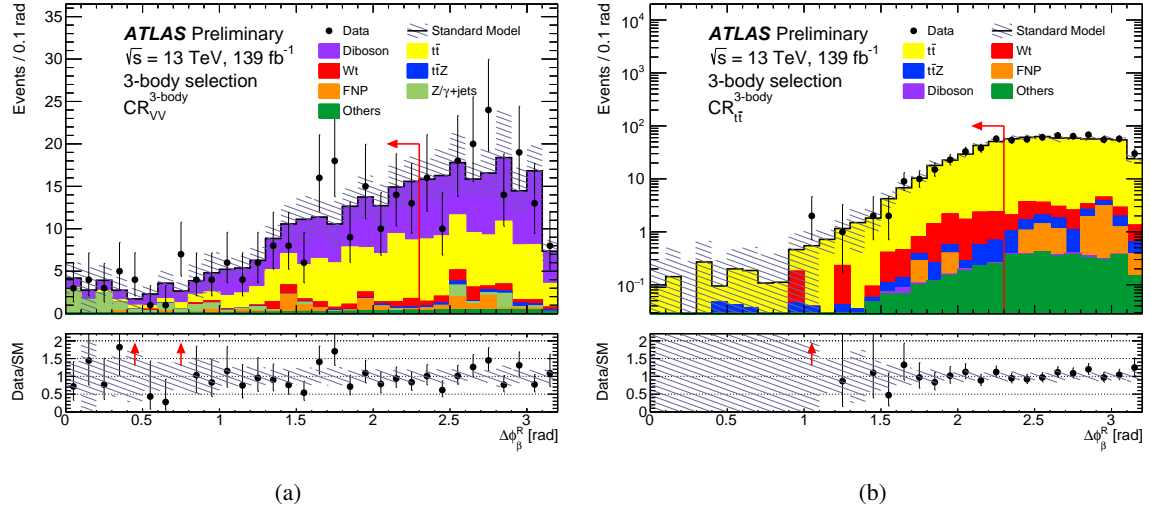


Figure 4: *Three-body selection.* Distributions of $\Delta\phi_\beta^R$ in the $CR_{VV}^{3\text{-body}}$ selection (a), and in the $CR_{t\bar{t}}^{3\text{-body}}$ selection (b), after the background fit. The contributions from all SM backgrounds are shown as a histogram stack. "Others" include contributions from VVV , $t\bar{t}t$, $t\bar{t}t\bar{t}$, $t\bar{t}W$, $t\bar{t}WW$, $t\bar{t}WZ$, $t\bar{t}H$, and tZ processes. The hatched bands represent the total statistical and detector-related systematic uncertainty. In the upper panels red arrows indicate the control region selection criteria. In the bottom panels red arrows show data outside the y-axis range.

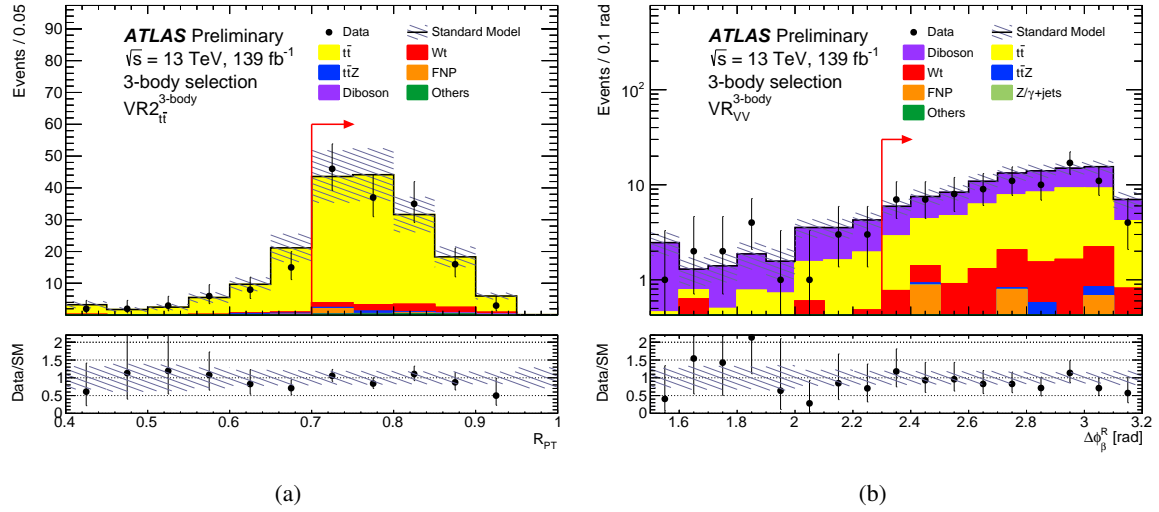


Figure 5: *Three-body selection.* Distributions of R_{PT} in the validation regions $VR(2)_{t\bar{t}}^{3\text{-body}}$ (a) and $\Delta\phi_\beta^R$ in the validation region $VR_{VV}^{3\text{-body}}$ (b), after the background fit. The contributions from all SM backgrounds are shown as a histogram stack. "Others" include contributions from VVV , $t\bar{t}t$, $t\bar{t}t\bar{t}$, $t\bar{t}W$, $t\bar{t}WW$, $t\bar{t}WZ$, $t\bar{t}H$, and tZ processes. The hatched bands represent the total statistical and detector-related systematic uncertainty. The rightmost bin of (a) includes overflow events. In the upper panels red arrows indicate the validation region selection criteria.

6.3 Estimation of the backgrounds in the four-body selection

The dominant irreducible SM background sources for the four-body selection are $t\bar{t}$ and diboson: these backgrounds are normalised in two dedicated, background enriched, control regions labelled as $\text{CR}_{t\bar{t}}^{4\text{-body}}$ and $\text{CR}_{VV}^{4\text{-body}}$. Some of the requirements defining the kinematics of the SRs are released in order to allow the selection of $t\bar{t}$ events in $\text{CR}_{t\bar{t}}^{4\text{-body}}$, while the $R_{2\ell}$ selection is adjusted to maintain a complete orthogonality with the SRs. The diboson contribution in $\text{CR}_{VV}^{4\text{-body}}$ is enhanced by limiting the number of jets in the event and the sub-leading jet p_T , and by the additional veto on the b -jets. The background predictions are tested in validation regions: $\text{VR}_{t\bar{t}}^{4\text{-body}}$ for $t\bar{t}$ validation and $\text{VR}_{VV}^{4\text{-body}}$ and $\text{VR}_{VV,3\ell}^{4\text{-body}}$ for diboson validation, these two latter selecting, respectively, events with two and three leptons in the final state. For the $\text{VR}_{VV,3\ell}^{4\text{-body}}$ region a new set of variables are defined to mimic the dibosons' kinematics in the signal regions. The two SFOS leptons with an invariant mass closest to m_Z are considered as the two leptons coming from the decay of the Z boson. The momentum of the lepton ($\mathbf{p}_{\ell_{\text{paired}}}^Z$) of the selected pair having the same electric charge of the non-paired lepton is added to the $\mathbf{p}_T^{\text{miss}}$ in order to define $E_{T,1\ell,\text{corr}}^{\text{miss}} = \left| \left(\mathbf{p}_T^{\text{miss}} + \mathbf{p}_{\ell_{\text{paired}}}^Z \right)_T \right|$ and $R_{\ell,\text{corr}}$ as the ratio of $E_{T,1\ell,\text{corr}}^{\text{miss}}$ and the two remaining leptons. The invariant mass of the remaining two leptons, called $m_{\ell\ell,\text{corr}}$, is also used. The definition of the control and validation regions used in the four-body selection is summarised in Table 10. In the $t\bar{t}$ control region the signal contamination is $\sim 1\%$ or less. In the $\text{CR}_{VV}^{4\text{-body}}$ typical signal contamination is about $\sim 1 - 2\%$, reaching the highest value of $\sim 5\%$ for top squark mass of ~ 400 GeV and lightest neutralino mass of ~ 310 GeV at the boundary of the region excluded by the previous analysis. Signal contamination in the validation regions is below 10%.

Table 11 shows the expected and observed numbers of events in each of the control and validation regions after the background fit. The normalisation factors extracted by the fit for the diboson and $t\bar{t}$ production processes are 1.00 ± 0.25 and 0.90 ± 0.12 respectively. The distributions of E_T^{miss} in $\text{CR}_{t\bar{t}}^{4\text{-body}}$ and $R_{2\ell}$ in $\text{CR}_{VV}^{4\text{-body}}$, after the background fit, are shown in Figure 6. The distributions of $p_T(\ell_2)$ in $\text{VR}_{t\bar{t}}^{4\text{-body}}$, n_{jets} in $\text{VR}_{VV}^{4\text{-body}}$ and $E_{T,1\ell,\text{corr}}^{\text{miss}}$ in $\text{VR}_{VV,3\ell}^{4\text{-body}}$, after the background fit, are shown in Figure 7. Good agreement between data and the SM predictions is observed.

Table 10: *Four-body selection*. Control and validation regions definition. The common selection defined in Section 5 also applies to all regions.

| | $\text{CR}_{t\bar{t}}^{4\text{-body}}$ | $\text{CR}_{VV}^{4\text{-body}}$ | $\text{VR}_{t\bar{t}}^{4\text{-body}}$ | $\text{VR}_{VV}^{4\text{-body}}$ | $\text{VR}_{VV,3\ell}^{4\text{-body}}$ |
|---|--|----------------------------------|--|----------------------------------|--|
| Lepton multiplicity | 2 | 2 | 2 | 2 | 3 |
| Lepton flavour | DF+SF | DF+SF | DF+SF | DF+SF | at least one SFOS pair |
| $p_T(\ell_1)$ [GeV] | < 100 | < 100 | < 100 | < 100 | < 100 |
| $p_T(\ell_2)$ [GeV] | < 50 | < 50 | < 50 | < 50 | < 100 |
| $p_T(\ell_3)$ [GeV] | – | – | – | – | < 100 |
| $m_{\ell\ell}$ [GeV] | > 10 | > 45 | > 10 | > 45 | > 10 |
| $ m_{\ell\ell} - m_Z $ [GeV] | – | > 10 for SF only | – | > 10 for SF only | – |
| E_T^{miss} [GeV] | > 350 | > 250 | > 250 | > 250 | > 250 |
| $p_T(j_1)$ [GeV] | > 150 | > 150 | > 150 | > 150 | > 150 |
| $\min \Delta R_{\ell_2, j_i}$ | > 1 | > 1 | > 1 | > 1 | > 1 |
| n_{jets} | – | ≤ 2 | – | ≤ 4 | < 5 |
| $n_{b\text{-jets}}$ | ≥ 2 | $= 0$ | ≥ 1 | $= 0$ | $= 0$ |
| $b\text{-tagged } j_1$ | – | – | True | – | – |
| $p_T(j_2)$ [GeV] | – | < 40 if j_2 exists | – | – | – |
| E_T^{miss} significance | > 10 | > 10 | > 10 | > 10 | > 5 |
| $p_{T,\text{boost}}^{\ell\ell}$ [GeV] | > 280 | > 280 | > 280 | > 280 | – |
| $R_{2\ell}$ | < 5 | < 4 | > 5 | $[4, 5]$ | – |
| $R_{2\ell 4j}$ | – | – | $[0.3, 0.38]$ | – | – |
| $E_{T,1\ell,\text{corr}}^{\text{miss}}$ [GeV] | – | – | – | – | > 300 |
| $R_{2\ell,\text{corr}}$ | – | – | – | – | > 5 |
| $m_{\ell\ell,\text{corr}}$ [GeV] | – | – | – | – | > 10 |

Table 11: *Four-body selection*. Background fit results for $\text{CR}_{t\bar{t}}^{4\text{-body}}$, $\text{CR}_{VV}^{4\text{-body}}$, $\text{VR}_{t\bar{t}}^{4\text{-body}}$, $\text{VR}_{VV}^{4\text{-body}}$ and $\text{VR}_{VV,3\ell}^{4\text{-body}}$. The ‘Others’ category contains the contributions from VVV , $t\bar{t}t$, $t\bar{t}t\bar{t}$, $t\bar{t}W$, $t\bar{t}WW$, $t\bar{t}WZ$, $t\bar{t}H$, and tZ . Combined statistical and systematic uncertainties are given. Entries marked ‘–’ indicate a negligible background contribution.

| | $\text{CR}_{t\bar{t}}^{4\text{-body}}$ | $\text{CR}_{VV}^{4\text{-body}}$ | $\text{VR}_{t\bar{t}}^{4\text{-body}}$ | $\text{VR}_{VV}^{4\text{-body}}$ | $\text{VR}_{VV,3\ell}^{4\text{-body}}$ |
|----------------------------|--|----------------------------------|--|----------------------------------|--|
| Observed events | 149 | 163 | 86 | 168 | 25 |
| Total (post-fit) SM events | 149 ± 12 | 162 ± 13 | 86 ± 20 | 173 ± 14 | 27 ± 5 |
| Post-fit, $t\bar{t}$ | 115 ± 13 | 39 ± 13 | 41 ± 19 | 57 ± 14 | – |
| Post-fit, diboson | 0.7 ± 0.5 | 89 ± 18 | 1.5 ± 0.6 | 75 ± 18 | 19 ± 6 |
| Wt | 27 ± 4 | 11.9 ± 1.8 | 18 ± 5 | 10.3 ± 0.8 | – |
| $Z/\gamma^* + \text{jets}$ | 0.18 ± 0.07 | 2.1 ± 1.1 | 2.1 ± 0.5 | 0.81 ± 0.35 | – |
| $t\bar{t}Z$ | 1.32 ± 0.34 | 0.18 ± 0.09 | 0.52 ± 0.17 | 0.41 ± 0.16 | 0.120 ± 0.029 |
| Others | 2.41 ± 0.17 | 0.30 ± 0.26 | 1.34 ± 0.20 | 1.2 ± 0.2 | 0.095 ± 0.028 |
| Fake and non-prompt | 2.3 ± 2.1 | 20 ± 4 | 20.7 ± 3.4 | 28 ± 5 | 7.9 ± 1.1 |

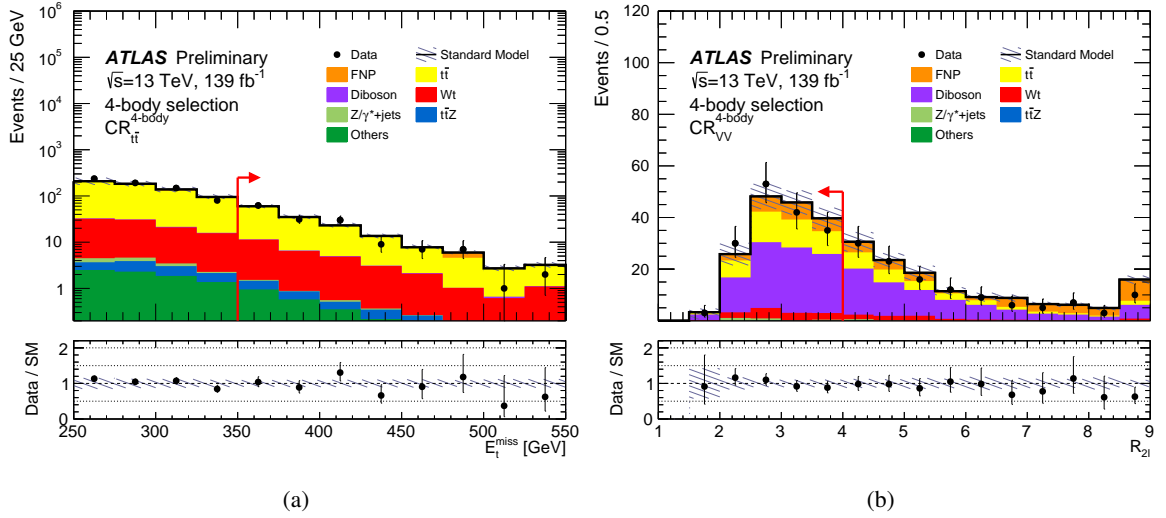


Figure 6: *Four-body selection*. Distributions of the (a) E_T^{miss} in $\text{CR}_{t\bar{t}}^{4\text{-body}}$ and (b) $R_{2\ell}$ in $\text{CR}_{VV}^{4\text{-body}}$ after the background fit. The contributions from all SM backgrounds are shown as a histogram stack. “Others” include contributions from VVV , $t\bar{t}t$, $t\bar{t}t\bar{t}$, $t\bar{t}W$, $t\bar{t}WW$, $t\bar{t}WZ$, $t\bar{t}H$, and tZ processes. The hatched bands represent the total statistical and detector-related systematic uncertainty. The rightmost bin of each plot includes overflow events. In the upper panels red arrows indicate the control region selection criteria.

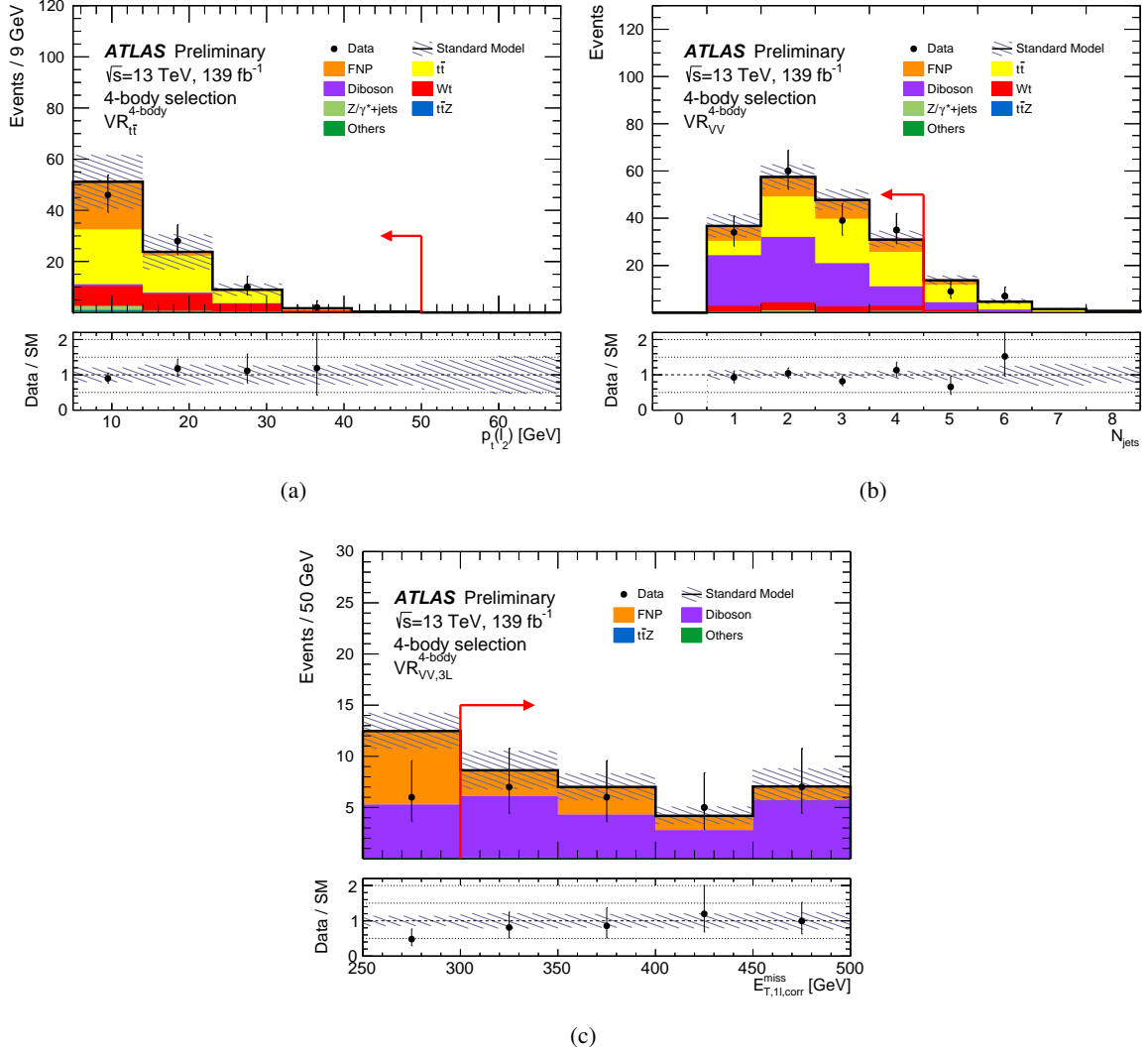


Figure 7: *Four-body selection.* Distributions of the (a) $p_T(\ell_2)$ in $\text{VR}_{t\bar{t}}^{4\text{-body}}$, (b) n_{jets} in $\text{VR}_{VV}^{4\text{-body}}$ and (c) $E_{T,1,\text{corr}}^{\text{miss}}$ in $\text{VR}_{VV,3\ell}^{4\text{-body}}$ after the background fit. The contributions from all SM backgrounds are shown as a histogram stack. "Others" include contributions from VVV , $t\bar{t}t$, $t\bar{t}t\bar{t}$, $t\bar{t}W$, $t\bar{t}WW$, $t\bar{t}WZ$, $t\bar{t}H$, and tZ processes. The hatched bands represent the total statistical and detector-related systematic uncertainty. The rightmost bin of each plot includes overflow events. In the upper panels red arrows indicate the validation region selection criteria.

7 Systematic uncertainties

Systematic uncertainties are evaluated for the signal and for the background predictions. The main experimental uncertainties in the yields of the reconstructed objects, the theoretical uncertainties on the processes yield, and the uncertainties related to the MC modelling of the SM backgrounds are described in this section. The statistical uncertainties in the simulated event samples are also taken into account.

The main sources of experimental uncertainty are related to the jet energy scale (JES) and the jet energy resolution (JER). The JES and JER uncertainties are derived as a function of the p_T and η of the jet, as well as of the pile-up conditions and the jet flavour composition of the selected jet sample [113]. Uncertainties associated to the modelling of the b -tagging efficiencies for b -jets, c -jets and light-flavour jets [114, 115] are also considered. Other detector-related systematic uncertainties, including those arising from lepton reconstruction efficiency, energy scale, energy resolution and in the modelling of the trigger efficiency [46, 52, 53, 116, 117], or the ones due to the pile-up reweighting and JVT are found to have a small impact on the results. The systematic uncertainties related to the modelling of E_T^{miss} in the simulation are estimated by propagating the uncertainties in the energy and momentum scale of electrons, muons and jets, as well as the uncertainties in the resolution and scale of the soft term [118].

Systematic uncertainties in the theoretical modelling of the observed final states can be broadly divided into uncertainties in the description of the parton-level final states (uncertainties in proton PDF, cross section, and strong coupling constant) and further uncertainties arising from the parton showering and hadronization processes that convert partons into the hadronic final states. The uncertainties in the modelling of the $t\bar{t}$ background are estimated by varying the renormalisation and factorisation scales, as well as the amount of initial- and final-state radiation used to generate the samples [119, 120]. Comparison between the yield obtained with POWHEG and MADGRAPH5_AMC@NLO [119] is used to estimate uncertainties for the event generator choice. For $t\bar{t}Z$ production, in the two-body and three-body selections, the effects of QCD scale uncertainties are evaluated using seven-point variations of the factorisation and renormalisation scales [121]. Uncertainties for additional radiation contributions (ISR,FSR) are evaluated comparing the nominal sample with one obtained with a PYTHIA tune enhancing the radiation [69]. Instead in the four-body selection, since the $t\bar{t}Z$ background contribution is minor, a total theoretical error of 14%, coming from the cross section uncertainty [122], is applied. For $t\bar{t}$ and $t\bar{t}Z$ production, the parton showering and hadronisation uncertainties are covered by the difference between samples obtained using the two different showering models implemented in PYTHIA and in HERWIG. Single top quark production via Wt -channel is a minor background in all the selections. Uncertainty in the acceptance due to the interference between $t\bar{t}$ and Wt production is assigned by comparing dedicated samples produced with POWHEG and PYTHIA using the Diagram Removal (DR) and the Diagram Subtraction (DS) approaches [123]. The modelling uncertainties for the diboson background are estimated using the seven-point variations of the renormalisation and factorisation scale. Additional uncertainties in the resummation (QSF) and matching (CKKM) scale between the matrix element generator and parton shower are computed varying the scale parameters in SHERPA [91]. For the other background processes which have minor contribution a conservative uncertainty is applied. These minor backgrounds are mainly $t\bar{t}WZ$ and ttW processes. A 30% uncertainty, driven by the DR versus DS of the $t\bar{t}WZ$ [124] process is applied in the 2-body and 3-body selection. For the 4-body selection a 22% uncertainty is applied due to the uncertainty on the $t\bar{t}W$ cross-section error [122]. For all the processes mentioned above the PDF uncertainties [125] were evaluated and found to be negligible.

Systematic uncertainties in the data driven FNP background estimate are expected due to potential differences in the FNP composition (heavy flavour, light flavour or photon conversions) between the regions defined in Section 6 and the CR^{FNP} used to extract the fake factor. A FNP systematic error is evaluated in

each of the regions varying the FNP composition in the CR^{FNP} to match the one of the considered analysis region. The statistical error is also included propagating the statistical uncertainty in the ratio used to compute the fake factor. For the 4-body selection, where the FNP lepton background is dominant, a FNP closure uncertainty is also evaluated considering the full difference between the data and FNP predictions as observed in a validation region with two same-sign leptons with kinematics similar to the four body selection. The closure uncertainty ranges between 13% and 33% in the regions where the FNP background is important.

A 1.7% uncertainty in the luminosity measurement is considered for all signal and background estimates that are directly derived from MC simulations [47].

Tables 12, 13 and 14 summarises the contributions of the different sources of systematic uncertainty in the total SM background predictions for the two-body, three-body and four-body signal regions. The total systematic uncertainty ranges between 14% and 26%, with the dominant sources being the MC statistical error, the JES and JER, the uncertainty on the background normalization and the theoretical uncertainties.

The SUSY signal cross-section uncertainty is evaluated from an envelope of the cross-section predictions using different PDF sets and factorisation and renormalisation scales as described in Ref [65]. The uncertainty in the DM production cross-section is derived from the scale variations and the PDF choices. The SUSY and DM theory signal uncertainties are computed from the variation of the radiation, renormalization, factorization and merging scale. These uncertainties are mostly relevant for the four-body selection and range between 2% and 24% depending on the mass difference $m(\tilde{t}_1) - m(\tilde{\chi}_1^0)$. For the DM signals the total systematic uncertainty is between 5% and 20%.

Table 12: *Two-body selection*. Sources of systematic uncertainty in the SM background estimates, after the background fits for the SF selection. The values are given as relative uncertainties in the total expected background event yields in the SRs. Entries marked ‘–’ indicate a contribution smaller than 1%. MC statistics refer to the statistical uncertainty from the simulated event samples. The individual components can be correlated and therefore do not necessarily add up in quadrature to the total systematic uncertainty.

| Signal Region | SR-SF ^{2-body} _{[110,120)} | SR-SF ^{2-body} _{[120,140)} | SR-SF ^{2-body} _{[140,160)} | SR-SF ^{2-body} _{[160,180)} | SR-SF ^{2-body} _{[180,220)} | SR-SF ^{2-body} _{[220,∞)} |
|---------------------------------------|--|--|--|--|--|--|
| Total SM background uncertainty | 19% | 20% | 17% | 15% | 15% | 20% |
| VV theoretical uncertainties | – | 2.4% | 3.5% | 4.9% | 4.4% | 7.1% |
| $t\bar{t}$ theoretical uncertainties | 10% | 11% | 6.2% | – | 1.7% | 2.7% |
| $t\bar{t}Z$ theoretical uncertainties | 1.0% | 2.2% | 4.2% | 5.2% | 5.0% | 11% |
| $t\bar{t}$ - Wt interference | – | – | – | – | 1.0% | 5.7% |
| Other theoretical uncertainties | 1.0% | 1.4% | 2.7% | 2.5% | 2.6% | 1.9% |
| MC statistical uncertainty | 5.1% | 5.4% | 7.0% | 7.7% | 9.9% | 8.7% |
| $t\bar{t}$ normalization | 7.6% | 4.8% | 1.0% | – | – | – |
| $t\bar{t}Z$ normalization | 1.1% | 3.2% | 5.6% | 7.2% | 6.4% | 4.8% |
| Jet energy scale | 11% | 6.7% | 9.6% | 2.0% | 3.4% | 2.0% |
| Jet energy resolution | 3.6% | 13% | 7.0% | 6.1% | 3.6% | 7.7% |
| E_T^{miss} modelling | 2.9% | 3.6% | 1.0% | 4.1% | 2.7% | 1.2% |
| Lepton modelling | 3.6% | 1.8% | 1.8% | 3.8% | 3.7% | 6.4% |
| Flavor tagging | 1.0% | 1.0% | 1.0% | 2.6% | 3.0% | 2.4% |
| Pile-up reweighting and JVT | – | 1.4% | 1.0% | 1.0% | 1.7% | – |
| Fake and non-prompt leptons | – | – | 1.1% | – | 2.8% | 4.3% |

Table 13: *Two-body selection*. Sources of systematic uncertainty in the SM background estimates, after the background fits for the DF selection. The values are given as relative uncertainties in the total expected background event yields in the SRs. Entries marked ‘–’ indicate a contribution smaller than 1%. MC statistics refer to the statistical uncertainty from the simulated event samples. The individual components can be correlated and therefore do not necessarily add up in quadrature to the total systematic uncertainty.

| Signal Region | SR-DF _[110,120] ^{2-body} | SR-DF _[120,140] ^{2-body} | SR-DF _[140,160] ^{2-body} | SR-DF _[160,180] ^{2-body} | SR-DF _[180,220] ^{2-body} | SR-DF _{[220,∞)} ^{2-body} |
|---------------------------------------|--|--|--|--|--|--|
| Total SM background uncertainty | 20% | 20% | 15% | 16% | 14% | 21% |
| VV theoretical uncertainties | 1.0% | 1.3% | 2.6% | 1.0% | 2.0% | 1.8% |
| $t\bar{t}$ theoretical uncertainties | 9.6% | 12% | 7.6% | – | 3.1% | – |
| $t\bar{t}Z$ theoretical uncertainties | 1.2% | 2.0% | 5.3% | 6.6% | 5.7% | 16% |
| $t\bar{t}$ - Wt interference | – | – | – | – | – | – |
| Other theoretical uncertainties | 1.0% | 1.2% | 2.8% | 3.2% | 2.7% | 3.3% |
| MC statistical uncertainty | 4.7% | 5.0% | 6.9% | 8.2% | 7.7% | 6.6% |
| $t\bar{t}$ normalization | 7.2% | 5.6% | 1.2% | – | – | – |
| $t\bar{t}Z$ normalization | 1.4% | 2.8% | 6.9% | 9.1% | 7.3% | 7.2% |
| Jet energy scale | 8.5% | 10% | 2.5% | 6.1% | 1.0% | 2.6% |
| Jet energy resolution | 13% | 6.6% | 6.2% | 4.3% | 5.3% | 2.0% |
| E_T^{miss} modelling | 3.5% | 6.1% | 1.0% | 2.2% | 2.2% | 1.0% |
| Lepton modelling | 1.5% | 1.1% | 1.6% | 1.3% | 1.3% | 1.0% |
| Flavor tagging | 1.0% | 1.0% | 1.3% | 2.0% | 1.0% | 1.0% |
| Pile-up reweighting and JVT | – | 1.6% | 1.0% | – | 1.0% | – |
| Fake and non-prompt leptons | – | 3.5% | – | – | 7.1% | 13% |

Table 14: *Three-body and four-body selections.* Sources of systematic uncertainty in the SM background estimates, after the background fits. The values are given as relative uncertainties in the total expected background event yields in the SRs. Entries marked ‘–’ indicate a contribution smaller than 1%. MC statistics refer to the statistical uncertainty from the simulated event samples. The individual components can be correlated and therefore do not necessarily add up in quadrature to the total systematic uncertainty.

| Signal Region | SR-DF _W ^{3-body} | SR-SF _W ^{3-body} | SR-DF _t ^{3-body} | SR-SF _t ^{3-body} | SR ^{4-body} _{Small Δm} | SR ^{4-body} _{Large Δm} |
|---------------------------------------|--------------------------------------|--------------------------------------|--------------------------------------|--------------------------------------|---|---|
| Total SM background uncertainty | 18% | 26% | 18% | 22% | 25% | 14% |
| VV theoretical uncertainties | 8.0% | 10% | 1.0% | 1.5% | 3.6% | 4.9% |
| $t\bar{t}$ theoretical uncertainties | 8.2% | 6.6% | 14% | 8.6% | 1.0% | 6.3% |
| $t\bar{t}Z$ theoretical uncertainties | – | – | 1.2% | 2.0% | – | – |
| $t\bar{t}$ - Wt interference | – | 1.0% | – | 1.1% | – | 2.4% |
| Other theoretical uncertainties | – | – | 1.4% | 1.6% | – | – |
| MC statistical uncertainty | 5.8% | 7.4% | 5.6% | 6.7% | 3.3% | 2.7% |
| VV normalization | 15% | 20% | 1.0% | 2.0% | 2.8% | 8.6% |
| $t\bar{t}$ normalization | 2.3% | 1.9% | 4.9% | 3.3% | 1.0% | 6.1% |
| $t\bar{t}Z$ normalization | – | – | 4.1% | 4.5% | – | – |
| Jet energy scale | 5.5% | 3.7% | 3.8% | 4.1% | 1.0% | 3.2% |
| Jet energy resolution | 2.3% | 11% | 9.0% | 18% | 1.3% | 3.5% |
| Lepton modelling | 1.3% | 2.0% | 1.0% | 2.5% | 1.3% | 3.3% |
| E_T^{miss} modelling | 1.1% | 2.2% | 3.0% | 1.8% | – | 1.0% |
| Flavor tagging | 3.1% | 2.9% | 1.6% | 1.0% | – | 1.3% |
| Pile-up reweighting and JVT | 1.0% | 1.0% | – | – | 1.0% | – |
| Fake and non-prompt leptons | 1.7% | – | – | 4.6% | 25% | – |

8 Results

A simultaneous likelihood fit is performed, for each one of the three different selections, using standard minimisation software packages, HistFitter and pyhf [106, 107]. For the semi-data driven backgrounds normalisation, only the CRs are considered in the background fit, while for the computation of the exclusion limits both CRs and SRs are included as constraining channels. The likelihood is a product of Poisson probability density functions (pdf), describing the observed number of events in each CR/SR, and Gaussian pdf distributions that describe the nuisance parameters associated with all the systematic uncertainties. Systematic uncertainties that are correlated between different samples are accounted for in the fit configuration by using the same nuisance parameter. The uncertainties are applied in each of the CRs and SRs and their effect is correlated for events across all regions in the fit.

The results of the background fit are shown in Figures 8-10 for all three analysis selections. In general good agreement, within about one standard deviation, is observed in all the SRs and VRs except in SR-DF_W^{3-body} where an underfluctuation is present.

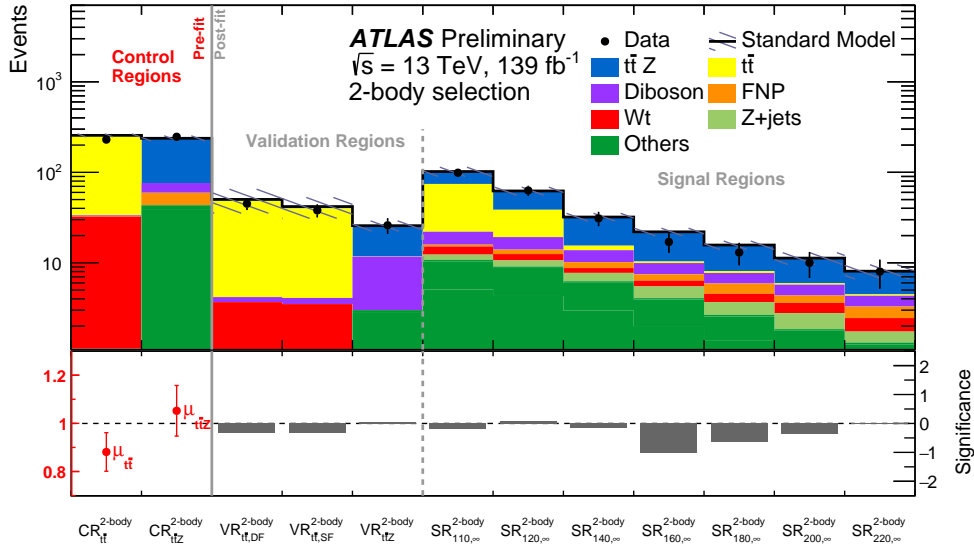


Figure 8: *Two-body selection*. Expected and observed yields are shown. The upper panel shows the observed number of events in each of the CRs, VRs and the inclusive SRs defined in the two-body selection, together with the expected SM backgrounds obtained before the fit in the CRs and after the fit in the VRs and SRs. "Others" include contributions from VVV , $t\bar{t}t$, $t\bar{t}t\bar{t}$, $t\bar{t}W$, $t\bar{t}WW$, $t\bar{t}WZ$, $t\bar{t}H$, and tZ processes. The shaded band represents the total uncertainty in the expected SM background. The lower panel shows the normalisation factors (left two bins) extracted in the CRs for the $t\bar{t}$ and $t\bar{t}Z$ processes, while, for the VRs and the inclusive SRs (right bins), the significance as defined in Ref. [126].

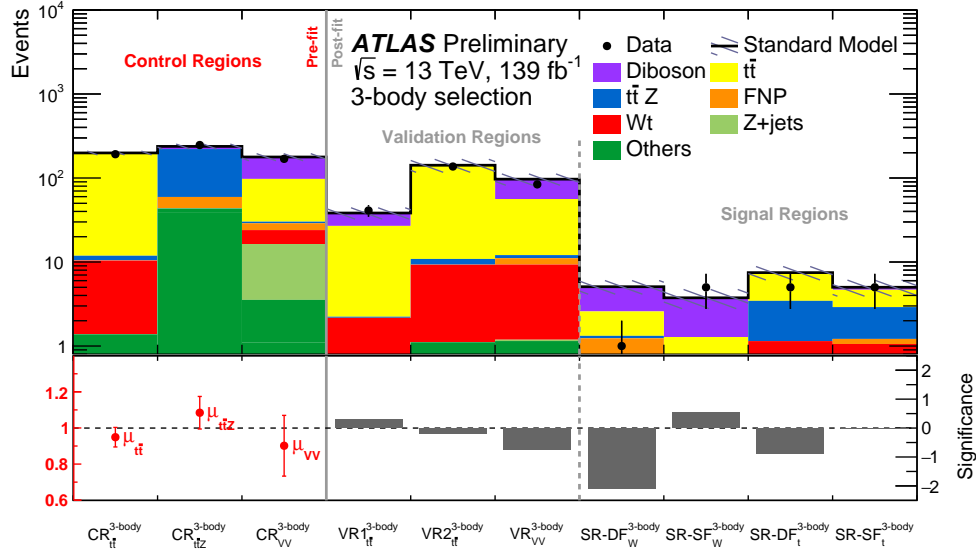


Figure 9: *Three-body selection*. Expected and observed yields are shown. The upper panel shows the observed number of events in each of the CRs, VRs and SRs defined in the three-body selection, together with the expected SM backgrounds obtained before the fit in the CRs and after the fit in the VRs and SRs. "Others" include contributions from VVV , $t\bar{t}t$, $t\bar{t}t\bar{t}$, $t\bar{t}W$, $t\bar{t}WW$, $t\bar{t}WZ$, $t\bar{t}H$, and tZ processes. The shaded band represents the total uncertainty in the expected SM background. The lower panel shows the normalisation factors (left three bins) extracted in the CRs for the $t\bar{t}$, $t\bar{t}Z$ and diboson processes, while, for the VRs and the SRs (right bins), the significance as defined in Ref. [126].

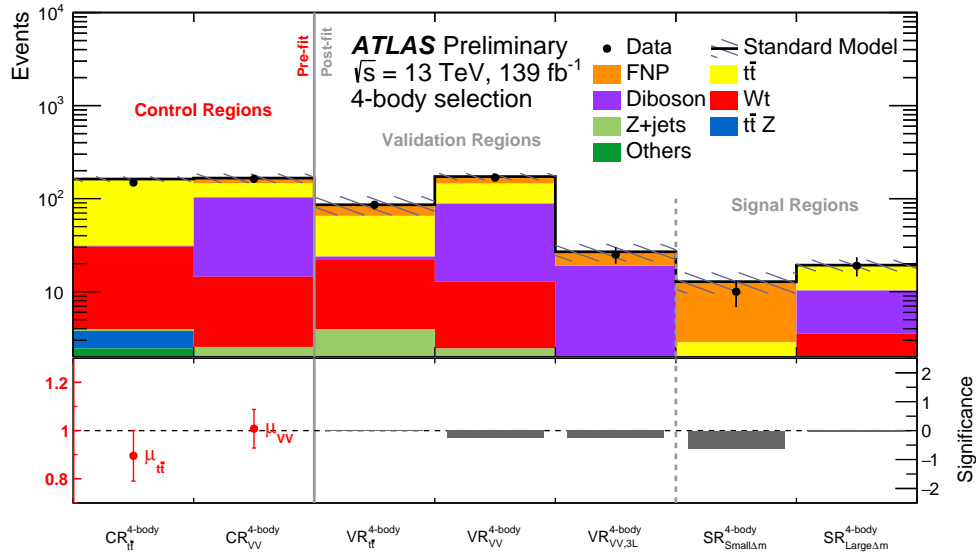


Figure 10: *Four-body selection*. Expected and observed yields are shown. The upper panel shows the observed number of events in each of the CRs, VRs and SRs defined in the three-body selection, together with the expected SM backgrounds obtained before the fit in the CRs and after the fit in the VRs and SRs. "Others" include contributions from VVV , $t\bar{t}t$, $t\bar{t}t\bar{t}$, $t\bar{t}W$, $t\bar{t}WW$, $t\bar{t}WZ$, $t\bar{t}H$, and tZ processes. The shaded band represents the total uncertainty in the expected SM background. The lower panel shows the normalisation factors (left two bins) extracted in the CRs for the $t\bar{t}$ and diboson processes, while, for the VRs and the SRs (right bins), the significance as defined in Ref. [126].

8.1 Two-body selection results

The estimated SM yields in the binned and inclusive SRs defined in the two-body selection are obtained with a background fit which simultaneously determine the normalisations of the background contributions from $t\bar{t}$ and $t\bar{t}Z$. Figure 11 shows the $m_{T2}^{\ell\ell}$ distribution for events satisfying all the selection criteria of the SR_{110,∞}^{2-body} (SF and DF) signal regions, after the background fit. Each bin corresponds to one of the binned SR. No significant excess over the SM prediction is observed, as can be seen from results shown in Tables 15,16 for the binned SRs.

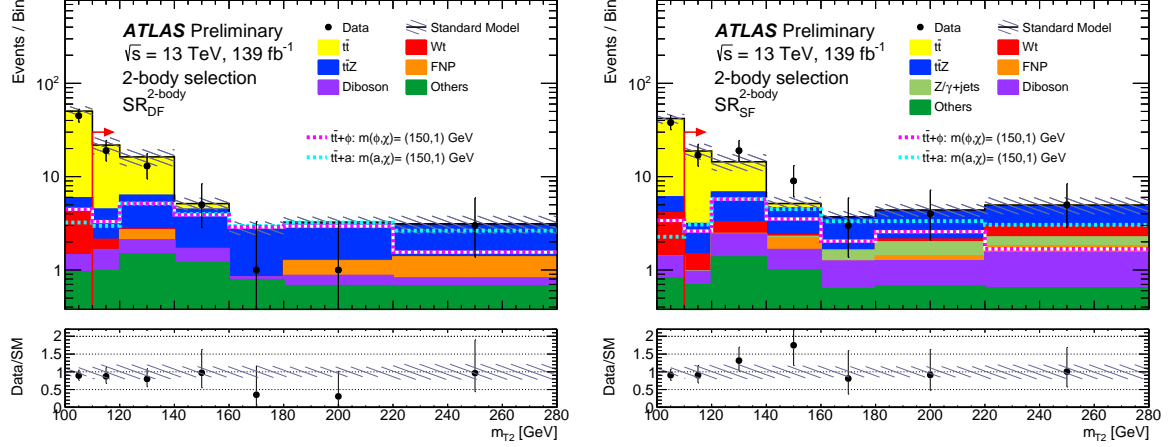


Figure 11: *Two-body selection*. Distributions of $m_{T2}^{\ell\ell}$ in SR_{110,∞}^{2-body} for different flavour (left) and same flavour (right) events satisfying the selection criteria of the given SR, except for the one on the represented variable, after the background fit. The contributions from all SM backgrounds are shown as a histogram stack. "Others" include contributions from VVV , $t\bar{t}t$, $t\bar{t}t\bar{t}$, $t\bar{t}W$, $t\bar{t}WW$, $t\bar{t}WZ$, $t\bar{t}H$, and tZ processes. The hatched bands represent the total statistical and systematic uncertainty. The rightmost bin of each plot includes overflow events. Reference dark matter signal models are overlayed for comparison. Red arrows in the upper panels indicate the signal region selection criteria.

Table 15: *Two-body selection*. Background fit results for the different flavour leptons binned SRs. The ‘Others’ category contains the contributions from VVV , $t\bar{t}t$, $t\bar{t}t\bar{t}$, $t\bar{t}W$, $t\bar{t}WW$, $t\bar{t}WZ$, $t\bar{t}H$, and tZ . Combined statistical and systematic uncertainties are given. Entries marked ‘–’ indicate a negligible background contribution.

| | SR-DF _[110,120] ^{2-body} | SR-DF _[120,140] ^{2-body} | SR-DF _[140,160] ^{2-body} | SR-DF _[160,180] ^{2-body} | SR-DF _[180,220] ^{2-body} | SR-DF _[220,∞] ^{2-body} |
|----------------------------|--|--|--|--|--|--|
| Observed events | 19 | 13 | 5 | 1 | 1 | 3 |
| Fitted bkg events | 22 ± 4 | 16.3 ± 3.2 | 5.1 ± 0.8 | 2.83 ± 0.45 | 3.25 ± 0.45 | 3.11 ± 0.67 |
| Post-fit, $t\bar{t}$ | 17 ± 4 | 10.0 ± 3.2 | 0.7 ± 0.5 | 0.01 ^{+0.10} _{-0.01} | 0.13 ± 0.11 | – |
| Post-fit, $t\bar{t} + Z$ | 2.3 ± 0.5 | 3.5 ± 0.7 | 2.7 ± 0.7 | 2.0 ± 0.4 | 1.9 ± 0.4 | 1.7 ± 0.6 |
| Wt | 0.47 ± 0.27 | 0.05 ^{+0.33} _{-0.05} | 0.025 ± 0.012 | – | 0.033 ± 0.013 | – |
| $Z/\gamma^* + \text{jets}$ | – | – | – | – | – | – |
| Diboson | 0.67 ± 0.27 | 0.61 ± 0.24 | 0.49 ± 0.16 | 0.05 ^{+0.07} _{-0.05} | 0.19 ± 0.13 | 0.14 ± 0.07 |
| Others | 0.97 ± 0.19 | 1.48 ± 0.28 | 1.19 ± 0.16 | 0.78 ± 0.12 | 0.68 ± 0.13 | 0.67 ± 0.11 |
| Fake and non-prompt | 0.0 ^{+0.5} _{-0.0} | 0.6 ± 0.6 | 0.0 ^{+0.5} _{-0.0} | 0.0 ^{+0.5} _{-0.0} | 0.37 ± 0.23 | 0.6 ± 0.4 |

Table 16: *Two-body selection*. Background fit results for the same flavour leptons binned SRs. The ‘Others’ category contains the contributions from VVV , $t\bar{t}t$, $t\bar{t}t\bar{t}$, $t\bar{t}W$, $t\bar{t}WW$, $t\bar{t}WZ$, $t\bar{t}H$, and tZ . Combined statistical and systematic uncertainties are given.

| | SR-SF _[110,120] ^{2-body} | SR-SF _[120,140] ^{2-body} | SR-SF _[140,160] ^{2-body} | SR-SF _[160,180] ^{2-body} | SR-SF _[180,220] ^{2-body} | SR-SF _{[220,∞)} ^{2-body} |
|----------------------------|--|--|--|--|--|--|
| Observed events | 17 | 19 | 9 | 3 | 4 | 5 |
| Fitted bkg events | 18.8 ± 3.5 | 14.4 ± 2.9 | 5.1 ± 0.9 | 3.7 ± 0.6 | 4.4 ± 0.7 | 5 ± 1 |
| Post-fit, $t\bar{t}$ | 15.7 ± 3.4 | 7.6 ± 2.3 | 0.6 ± 0.4 | $0.007^{+0.020}_{-0.007}$ | 0.10 ± 0.08 | $0.16^{+0.18}_{-0.16}$ |
| Post-fit, $t\bar{t} + Z$ | 1.65 ± 0.35 | 3.5 ± 0.7 | 2.2 ± 0.5 | 2.1 ± 0.4 | 2.18 ± 0.45 | 1.9 ± 0.6 |
| Wt | 0.5 ± 0.5 | 0.8 ± 0.8 | 0.10 ± 0.04 | $0.018^{+0.019}_{-0.018}$ | 0.12 ± 0.06 | 0.71 ± 0.29 |
| $Z/\gamma^* + \text{jets}$ | 0.020 ± 0.014 | 0.044 ± 0.003 | $0.07^{+0.17}_{-0.07}$ | 0.38 ± 0.13 | 0.60 ± 0.33 | 0.4 ± 0.4 |
| Diboson | 0.27 ± 0.20 | 1.0 ± 0.6 | 0.65 ± 0.24 | 0.6 ± 0.4 | 0.59 ± 0.28 | 0.9 ± 0.5 |
| Others | 0.69 ± 0.13 | 1.37 ± 0.21 | 0.99 ± 0.16 | 0.63 ± 0.11 | 0.67 ± 0.14 | 0.64 ± 0.10 |
| Fake and non-prompt | $0.0^{+0.4}_{-0.0}$ | $0.0^{+0.4}_{-0.0}$ | 0.56 ± 0.06 | $0.0^{+0.7}_{-0.0}$ | 0.15 ± 0.12 | 0.28 ± 0.21 |

8.2 Three-body selection results

The dominant background processes yield in the three-body selection are from production of diboson, $t\bar{t}$ and $t\bar{t}Z$, are determined with a simultaneous fit. Figure 12 shows the distributions of M_{Δ}^R in the SR _{Δ^W} ^{3-body} (top) and in the SR _{t} ^{3-body} (bottom), for events satisfying all the selection criteria except the represented variable, after the background fit. Table 17 shows the observed events in each signal regions and the SM background estimations. No excess over the SM prediction is observed while an underfluctuation of 2σ is observed in SR-DF _{W} ^{3-body} which is also visible in Figure 12(a).

Table 17: *Three-body selection*. Observed event yield and background fit results for the three-body selection SRs. The ‘Others’ category contains contributions from VVV , $t\bar{t}t$, $t\bar{t}t\bar{t}$, $t\bar{t}W$, $t\bar{t}WW$, $t\bar{t}WZ$, $t\bar{t}H$, and tZ . Combined statistical and systematic uncertainties are given. Entries marked ‘–’ indicate a negligible background contribution.

| | SR-DF _{W} ^{3-body} | SR-SF _{W} ^{3-body} | SR-DF _{t} ^{3-body} | SR-SF _{t} ^{3-body} |
|----------------------------|---|---|---|---|
| Observed events | 1 | 5 | 5 | 5 |
| Total (post-fit) SM events | 5.1 ± 1.0 | 4.0 ± 1.0 | 7.5 ± 1.4 | 5.0 ± 1.1 |
| Post-fit, $t\bar{t}$ | 1.3 ± 0.5 | 0.76 ± 0.32 | 3.9 ± 1.1 | 1.8 ± 0.7 |
| Post-fit, $t\bar{t} + Z$ | 0.085 ± 0.034 | 0.08 ± 0.05 | 2.3 ± 0.4 | 1.69 ± 0.35 |
| Post-fit, diboson | 2.5 ± 1.0 | 2.5 ± 1.0 | 0.17 ± 0.09 | 0.34 ± 0.14 |
| Wt | 0.30 ± 0.05 | 0.211 ± 0.030 | $0.4^{+0.5}_{-0.4}$ | 0.54 ± 0.19 |
| $Z/\gamma^* + \text{jets}$ | – | 0.044 ± 0.019 | – | $0.015^{+0.027}_{-0.015}$ |
| Others | 0.232 ± 0.020 | 0.25 ± 0.05 | 0.70 ± 0.12 | 0.49 ± 0.08 |
| Fake and non-prompt | 0.70 ± 0.09 | $0.00^{+0.25}_{-0.00}$ | $0.00^{+0.23}_{-0.00}$ | $0.16^{+0.23}_{-0.16}$ |

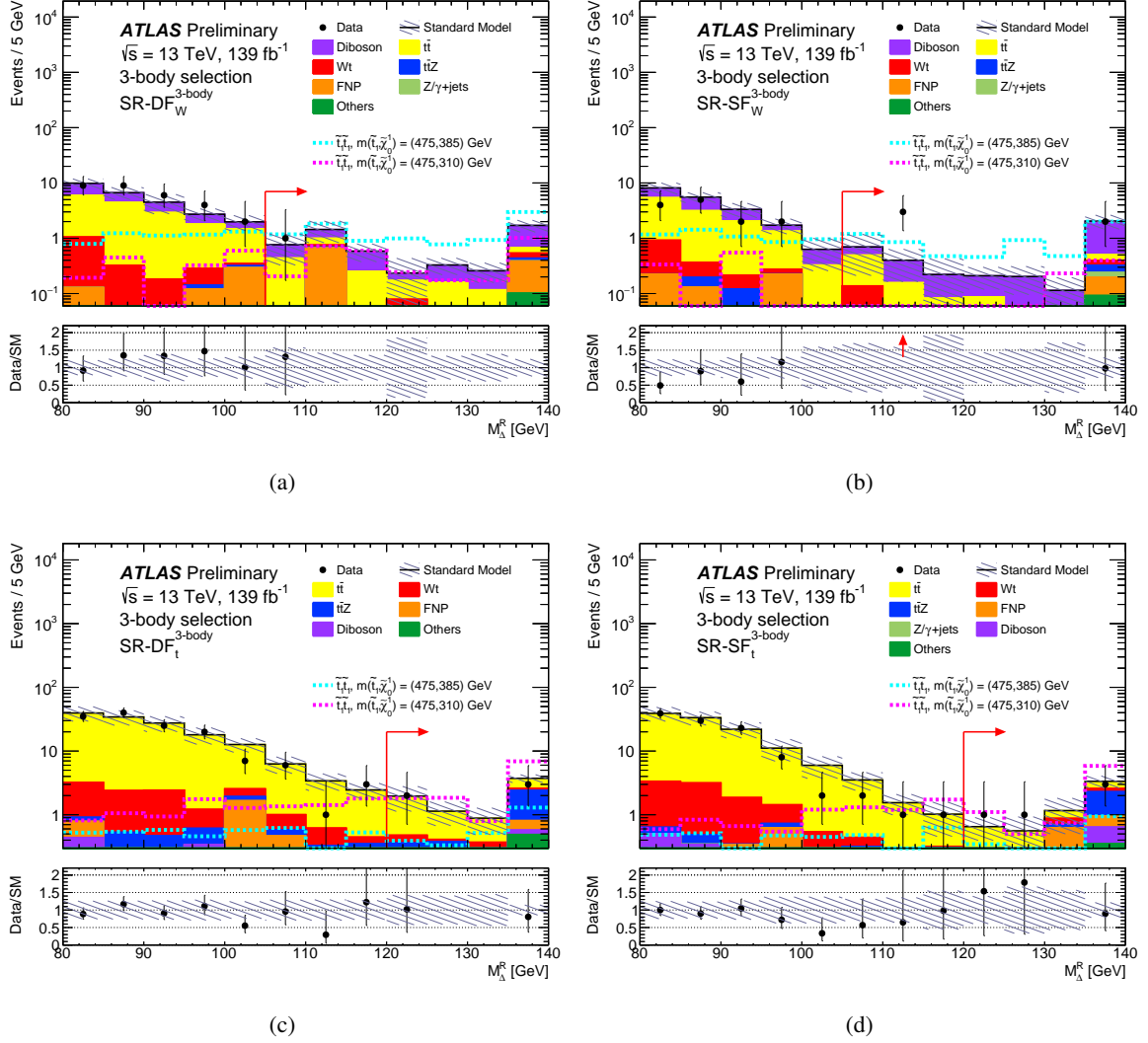


Figure 12: *Three-body selection.* Distributions of M_Δ^R in (a,b) $\text{SR}_W^{3\text{-body}}$ and (c,d) $\text{SR}_t^{3\text{-body}}$ for same flavour (left) and different flavour (right) events satisfying the selection criteria of the given SR, except for the one on the represented variable, after the background fit. The contributions from all SM backgrounds are shown as a histogram stack. "Others" include contributions from VVV , $t\bar{t}t$, $t\bar{t}t\bar{t}$, $t\bar{t}W$, $t\bar{t}WW$, $t\bar{t}WZ$, $t\bar{t}H$, and tZ processes. The hatched bands represent the total statistical and systematic uncertainty. The rightmost bin of each plot includes overflow events. Reference top squark pair production signal models are overlaid for comparison. Red arrows in the upper panels indicate the signal region selection criteria. In the bottom panels red arrows show data outside the y-axis range.

8.3 Four-body selection results

The estimated SM yields in $\text{SR}_{\text{Small } \Delta m}^{4\text{-body}}$ and $\text{SR}_{\text{Large } \Delta m}^{4\text{-body}}$ are determined with the background fit that provide the normalisation factors for $t\bar{t}$ and diboson production. Figure 13 shows the distributions of E_T^{miss} in the $\text{SR}_{\text{Small } \Delta m}^{4\text{-body}}$ (a) and $R_{2\ell 4j}$ in the $\text{SR}_{\text{Large } \Delta m}^{4\text{-body}}$ (b) for events satisfying the selection criteria of the given SR, except the ones on the represented variable, after the background fit. The background fit results are

shown in Table 18. The observed yield in the SR is within one standard deviation from the background prediction.

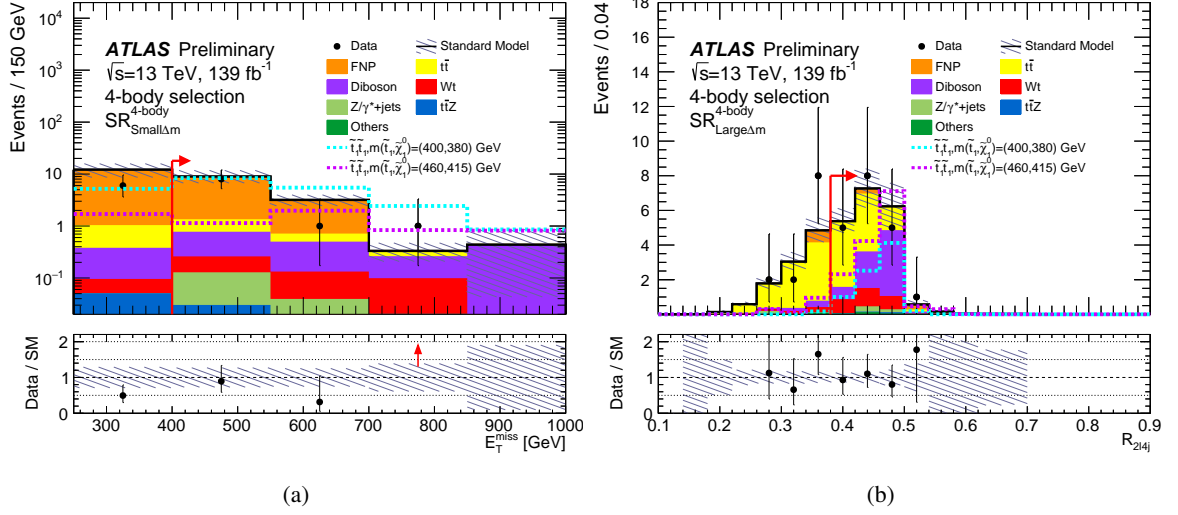


Figure 13: *Four-body selection*. (a) distributions of E_T^{miss} in $\text{SR}_{\text{Small } \Delta m}^{4\text{-body}}$ and (b) distribution of $R_{2\ell 4j}$ in $\text{SR}_{\text{Large } \Delta m}^{4\text{-body}}$ for events satisfying the selection criteria of the given SR, except for the one on the represented variable, after the background fit. The contributions from all SM backgrounds are shown as a histogram stack. "Others" include contributions from VVV , $t\bar{t}t$, $t\bar{t}t\bar{t}$, $t\bar{t}W$, $t\bar{t}WW$, $t\bar{t}WZ$, $t\bar{t}H$, and $t\bar{t}Z$ processes. The hatched bands represent the total statistical and systematic uncertainty. The rightmost bin of each plot includes overflow events. Reference top squark pair production signal models are overlayed for comparison. Red arrows in the upper panel indicate the signal region selection criteria. In the bottom panels red arrows show data outside the y-axis range.

Table 18: *Four-body selection*. Observed event yield and background fit results for $\text{SR}_{\text{Small } \Delta m}^{4\text{-body}}$ and $\text{SR}_{\text{Large } \Delta m}^{4\text{-body}}$. The 'Others' category contains the contributions from VVV , $t\bar{t}t$, $t\bar{t}t\bar{t}$, $t\bar{t}W$, $t\bar{t}WW$, $t\bar{t}WZ$, $t\bar{t}H$, and $t\bar{t}Z$. Combined statistical and systematic uncertainties are given.

| | $\text{SR}_{\text{Small } \Delta m}^{4\text{-body}}$ | $\text{SR}_{\text{Large } \Delta m}^{4\text{-body}}$ |
|----------------------------|--|--|
| Observed events | 10 | 19 |
| Total (post-fit) SM events | 12.8 ± 3.2 | 19.3 ± 2.7 |
| Post-fit, $t\bar{t}$ | 0.87 ± 0.26 | 8.7 ± 1.5 |
| Post-fit, diboson | 1.5 ± 0.5 | 6.8 ± 2.3 |
| Wt | 0.32 ± 0.08 | 2.7 ± 0.5 |
| $Z/\gamma^* + \text{jets}$ | 0.128 ± 0.023 | 0.46 ± 0.19 |
| $t\bar{t}Z$ | 0.047 ± 0.010 | 0.126 ± 0.033 |
| Others | $0.019^{+0.021}_{-0.019}$ | 0.26 ± 0.07 |
| Fake and non-prompt | 10.0 ± 3.1 | 0.24 ± 0.09 |

9 Interpretation

No excess is observed in the data with respect to the MC expected background. The analysis results are therefore interpreted in terms of model-independent upper limits on the visible cross section (σ_{vis}) of new physics, defined as the ratio between the upper limit at 95% CL on the number of signal events (S^{95}) and the integrated luminosity, and in terms of exclusion limits in the masses parameters plane of our simplified model. For the two-body selection the upper limits are derived using the inclusive SRs.

The upper limits on σ_{vis} are derived, in each SR, by performing a model-independent hypothesis test, which introduces a free signal as an additional process to be constrained by the observed yield. The CL_s method [127] is used to derive all the exclusion confidence levels. Model-independent upper limits are presented in Table 19. These limits assume negligible signal contamination in the CRs resulting in a more conservative result when comparing with model-dependent limits where a small signal contamination is allowed in the CRs.

Table 19: Model-independent 95% CL upper limits on the visible cross-section (σ_{vis}) of new physics, the visible number of signal events (S_{obs}^{95}), the visible number of signal events (S_{exp}^{95}) given the expected number of background events (and $\pm 1\sigma$ excursions of the expected number), and the discovery p -value ($p(s = 0)$), all calculated with pseudo-experiments, are shown for each SRs. The p -value is reported as 0.5 if the observed yield is smaller than that predicted.

| Selection | Signal Region | σ_{vis} [fb] | S_{obs}^{95} | S_{exp}^{95} | $p(s = 0)$ |
|------------|--|----------------------------|-----------------------|-----------------------|------------|
| Two-body | SR $_{110,\infty}^{2\text{-body}}$ | 0.21 | 29.3 | 31^{+11}_{-8} | 0.5 |
| | SR $_{120,\infty}^{2\text{-body}}$ | 0.15 | 21.4 | 21^{+8}_{-6} | 0.40 |
| | SR $_{140,\infty}^{2\text{-body}}$ | 0.10 | 13.2 | 14^{+5}_{-4} | 0.5 |
| | SR $_{160,\infty}^{2\text{-body}}$ | 0.06 | 8.2 | $11^{+5}_{-3.0}$ | 0.5 |
| | SR $_{180,\infty}^{2\text{-body}}$ | 0.06 | 7.9 | $9.6^{+3.8}_{-2.8}$ | 0.5 |
| | SR $_{200,\infty}^{2\text{-body}}$ | 0.06 | 7.6 | $8.4^{+3.6}_{-2.3}$ | 0.5 |
| | SR $_{220,\infty}^{2\text{-body}}$ | 0.05 | 7.6 | $7.5^{+3.1}_{-2.0}$ | 0.5 |
| Three-body | SR-DF $_W^{3\text{-body}}$ | 0.023 | 3.2 | $5.7^{+2.3}_{-1.5}$ | 0.5 |
| | SR-SF $_W^{3\text{-body}}$ | 0.05 | 7.0 | $5.6^{+2.3}_{-1.5}$ | 0.27 |
| | SR-DF $_t^{3\text{-body}}$ | 0.04 | 5.5 | $6.9^{+2.9}_{-1.9}$ | 0.5 |
| | SR-SF $_t^{3\text{-body}}$ | 0.04 | 6.3 | $6.1^{+2.6}_{-1.6}$ | 0.5 |
| Four-body | SR $_{\text{Small } \Delta m}^{4\text{-body}}$ | 0.06 | 8.2 | $9.6^{+3.8}_{-2.5}$ | 0.5 |
| | SR $_{\text{Large } \Delta m}^{4\text{-body}}$ | 0.08 | 11.1 | $11.1^{+4.5}_{-3.0}$ | 0.5 |

Model-dependent limits are computed for the various signal scenarios considered in the analysis. The hypothesis tests are performed including the expected signal yield and its associated uncertainties in the CRs and SRs. All limits are quoted at 95% CL with the CL_s method. When setting limits, the two-body selection binned SRs SR-DF $_{x,y}^{2\text{-body}}$ and SR-SF $_{x,y}^{2\text{-body}}$ regions are statistically combined. Similarly, the SR-DF $_W^{3\text{-body}}$, SR-SF $_W^{3\text{-body}}$, SR-DF $_t^{3\text{-body}}$, and SR-SF $_t^{3\text{-body}}$ signal regions are statistically combined for

the three-body selection, as also $\text{SR}_{\text{Small } \Delta m}^{4\text{-body}}$ and $\text{SR}_{\text{Large } \Delta m}^{4\text{-body}}$ for the four-body selection.

Limits for simplified models in which pair-produced \tilde{t}_1 decay with 100% branching ratio into a top quark and $\tilde{\chi}_1^0$ are shown in the \tilde{t}_1 – $\tilde{\chi}_1^0$ mass plane in Figure 14. The exclusion contour is obtained by the overlap of the ones derived from the three selections separately. Top squark masses up to 1 TeV are excluded for a massless lightest neutralino. Neutralino masses up to 500 GeV are excluded for $m(\tilde{t}_1)$ above the top quark production kinematical limit. In the three-body decay region, top squark masses are excluded up to 600 GeV for $\Delta m(\tilde{t}_1, \tilde{\chi}_1^0) = 120$ GeV, up to 550 GeV for $\Delta m(\tilde{t}_1, \tilde{\chi}_1^0)$ close to the top quark mass and up to 430 GeV for $\Delta m(\tilde{t}_1, \tilde{\chi}_1^0)$ close to the W boson mass. In the four-body decay region, top squark masses are excluded up to 540 GeV for $\Delta m(\tilde{t}_1, \tilde{\chi}_1^0) = 40$ GeV. Top squark decay around the W boson kinematical production limit is not fully excluded by the overlap between the four-body and three-body selections for $m(\tilde{t}_1)$ above 400 GeV. The four-body selection loses sensitivity for $\Delta m(\tilde{t}, \tilde{\chi}_1^0) \gtrsim m(W)$ due to the upper bound of the sub-leading lepton p_T while, for the three body selection, the M_{Δ}^R requirement suppresses the sensitivity for $\Delta m(\tilde{t}, \tilde{\chi}_1^0) \lesssim m(W)$ because of the smaller mass splitting. The three-body and two-body overlap in the sensitivity provides exclusion coverage around the top quark production kinematical limit up to $m(\tilde{t}_1)$ of 540 GeV.

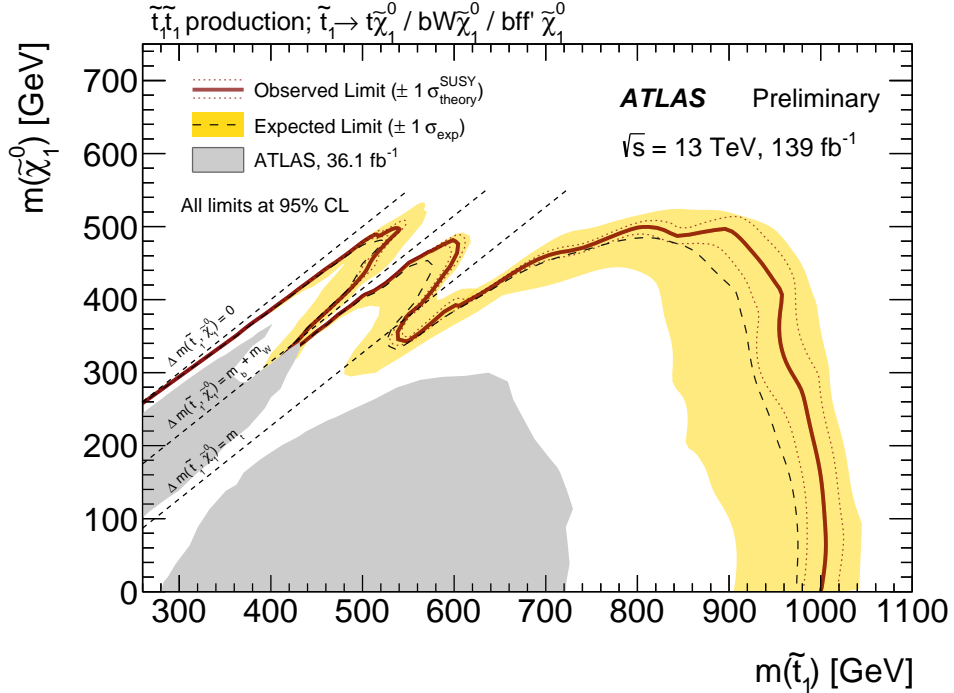


Figure 14: Exclusion limit contour (95% CL) for a simplified model assuming \tilde{t}_1 pair production, decaying via $\tilde{t}_1 \rightarrow t^{(*)} \tilde{\chi}_1^0$ with 100% branching ratio. The dashed lines and the shaded bands are the expected limit and its $\pm 1\sigma$ uncertainty. The thick solid lines are the observed limits for the central value of the signal cross-section. The expected and observed limits do not include the effect of the theoretical uncertainties in the signal cross-section. The dotted lines show the effect on the observed limit when varying the signal cross-section by $\pm 1\sigma$ of the theoretical uncertainty.

Figure 15 shows upper limits at 95% CL on the observed signal cross-section scaled to the theoretical signal cross-section for coupling $g = g_q = g_\chi = 1$, denoted by $\sigma/\sigma(g = 1.0)$. These limits are obtained as a function of the mediator mass, assuming a specific DM particle mass of 1 GeV (Figure 15). Both

the scalar and pseudoscalar mediator cases are considered. The sensitivity is approximately constant for mediator masses below 100 GeV, excluding the $g = 1$ assumption for scalar (pseudoscalar) mediator masses up to 250 (300) GeV.

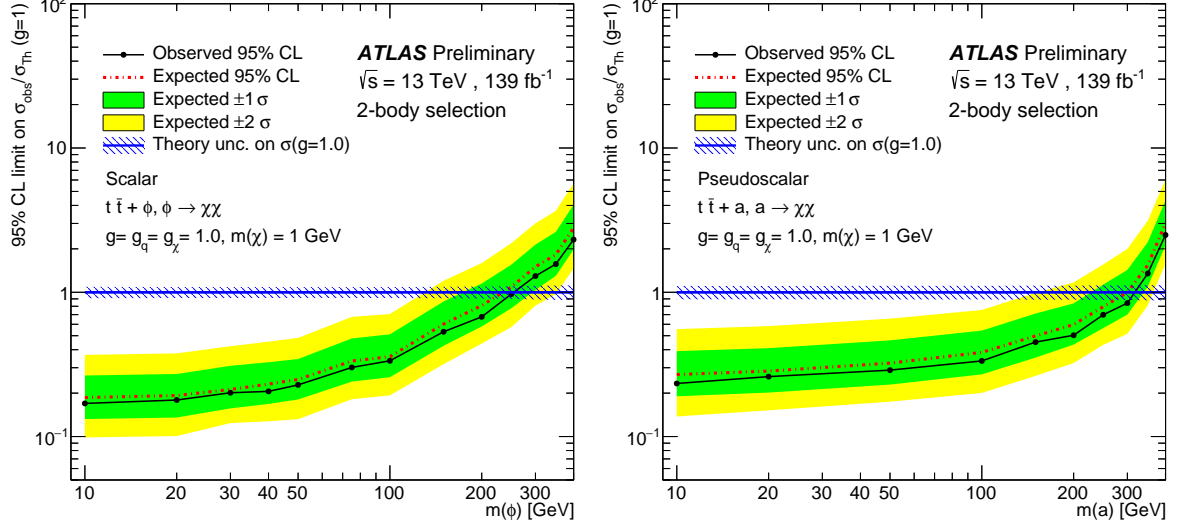


Figure 15: Exclusion limits for $t\bar{t} + \phi$ scalar (left) and $t\bar{t} + a$ pseudoscalar (right) models as a function of the mediator mass for a DM particle mass of $m(\chi) = 1$ GeV. The limits are calculated at 95% CL and are expressed in terms of the ratio of the excluded cross-section to the nominal cross-section for a coupling assumption of $g = g_q = g_\chi = 1$. The solid (dashed) lines shows the observed (expected) exclusion limits.

10 Conclusion

This paper reports the results of a search for direct top squark pair production and for dark matter in a final state containing two leptons with opposite electric charge, jets and missing transverse momentum. The search uses an integrated luminosity of 139 fb^{-1} of proton–proton collisions at $\sqrt{s} = 13 \text{ TeV}$, as collected by the ATLAS experiment at the Large Hadron Collider during Run 2 (2015–2018).

A significant improvement in sensitivity with respect to previous results is obtained using the new discriminating variable E_T^{miss} significance. Moreover in the small $\Delta m(\tilde{t}_1, \tilde{\chi}_1^0)$ region, an important gain in sensitivity is achieved by lowering the leptons' p_T threshold for selected leptons.

Data are found to be consistent with the Standard Model predictions. Assuming direct \tilde{t}_1 production and decay with 100% branching ratio into three different simplified models with the top squark decaying in two-bodies $\tilde{t}_1 \rightarrow t\tilde{\chi}_1^0$, in three bodies $\tilde{t}_1 \rightarrow bW\tilde{\chi}_1^0$, and in four bodies $\tilde{t}_1 \rightarrow b\ell\nu\tilde{\chi}_1^0$, constraints at 95% confidence level are placed on the minimum mass of \tilde{t}_1 and $\tilde{\chi}_1^0$ up to about 1 TeV, and 500 GeV respectively, extending the previous ATLAS limits obtained in a two-lepton final state with a unique sensitivity in the mass region where the decay $\tilde{t}_1 \rightarrow t\tilde{\chi}_1^0$ becomes kinematically allowed. For the dark matter, assuming spin-0 mediator production in association with a pair of top quarks and decay with 100% branching ratio into a pair of dark-matter particles constraints at 95% confidence level are set on the minimum scalar mediator masses up to about 250 GeV.

References

- [1] H. Goldberg, *Constraint on the Photino Mass from Cosmology*, [Phys. Rev. Lett. **50** \(1983\) 1419](#), Erratum: [Phys. Rev. Lett. **103** \(2009\) 099905](#).
- [2] J. Ellis, J. Hagelin, D. V. Nanopoulos, K. A. Olive and M. Srednicki, *Supersymmetric relics from the big bang*, [Nucl. Phys. B **238** \(1984\) 453](#).
- [3] Y. Golfand and E. Likhtman, *Extension of the Algebra of Poincare Group Generators and Violation of P Invariance*, [JETP Lett. **13** \(1971\) 323](#), [[Pisma Zh. Eksp. Teor. Fiz. **13** \(1971\) 452](#)].
- [4] D. Volkov and V. Akulov, *Is the neutrino a goldstone particle?*, [Phys. Lett. B **46** \(1973\) 109](#).
- [5] J. Wess and B. Zumino, *Supergauge transformations in four dimensions*, [Nucl. Phys. B **70** \(1974\) 39](#).
- [6] J. Wess and B. Zumino, *Supergauge invariant extension of quantum electrodynamics*, [Nucl. Phys. B **78** \(1974\) 1](#).
- [7] S. Ferrara and B. Zumino, *Supergauge invariant Yang-Mills theories*, [Nucl. Phys. B **79** \(1974\) 413](#).
- [8] A. Salam and J. Strathdee, *Super-symmetry and non-Abelian gauges*, [Phys. Lett. B **51** \(1974\) 353](#).
- [9] G. R. Farrar and P. Fayet, *Phenomenology of the production, decay, and detection of new hadronic states associated with supersymmetry*, [Phys. Lett. B **76** \(1978\) 575](#).
- [10] P. Fayet, *Supersymmetry and Weak, Electromagnetic and Strong Interactions*, [Phys. Lett. B **64** \(1976\) 159](#).
- [11] P. Fayet, *Spontaneously Broken Supersymmetric Theories of Weak, Electromagnetic and Strong Interactions*, [Phys. Lett. B **69** \(1977\) 489](#).
- [12] F. Zwicky, *Die Rotverschiebung von extragalaktischen Nebeln*, [Helv. Phys. Acta **6** \(1933\) 110](#).
- [13] G. Bertone, D. Hooper and J. Silk, *Particle dark matter: evidence, candidates and constraints*, [Phys. Rept. **405** \(2005\) 279](#), arXiv: [hep-ph/0404175](#).
- [14] G. Steigman and M. S. Turner, *Cosmological constraints on the properties of weakly interacting massive particles*, [Nucl. Phys. B **253** \(1985\) 375](#).
- [15] J. Goodman and W. Shepherd, *LHC Bounds on UV-Complete Models of Dark Matter*, 2011, arXiv: [1111.2359 \[hep-ph\]](#).
- [16] J. Alwall, P. Schuster and N. Toro, *Simplified models for a first characterization of new physics at the LHC*, [Phys. Rev. D **79** \(2009\) 075020](#), arXiv: [0810.3921 \[hep-ph\]](#).
- [17] D. Alves et al., *Simplified models for LHC new physics searches*, [J. Phys. G **39** \(2012\) 105005](#), arXiv: [1105.2838 \[hep-ph\]](#).
- [18] D. Abercrombie et al., *Dark Matter benchmark models for early LHC Run-2 Searches: Report of the ATLAS/CMS Dark Matter Forum*, [Phys. Dark Univ. **26** \(2019\) 100371](#), arXiv: [1507.00966 \[hep-ex\]](#).
- [19] M. R. Buckley, D. Feld and D. Goncalves, *Scalar simplified models for dark matter*, [Phys. Rev. D **91** \(2015\)](#), arXiv: [1410.6497 \[hep-ph\]](#).
- [20] U. Haisch and E. Re, *Simplified dark matter top-quark interactions at the LHC*, [JHEP **06** \(2015\) 078](#), arXiv: [1503.00691 \[hep-ph\]](#).
- [21] G. D'Ambrosio, G. Giudice, G. Isidori and A. Strumia, *Minimal Flavour Violation: an effective field theory approach*, [Nucl. Phys. B **645** \(2002\) 155](#), arXiv: [hep-ph/0207036](#).

- [22] ATLAS Collaboration, *Search for dark matter produced in association with bottom or top quarks in $\sqrt{s} = 13$ TeV pp collisions with the ATLAS detector*, *Eur. Phys. J. C* **78** (2018) 18, arXiv: [1710.11412 \[hep-ex\]](#).
- [23] ATLAS Collaboration, *Search for direct top squark pair production in final states with two leptons in $\sqrt{s} = 13$ TeV pp collisions with the ATLAS detector*, *Eur. Phys. J. C* **77** (2017) 898, arXiv: [1708.03247 \[hep-ex\]](#).
- [24] ATLAS Collaboration, *Object-based missing transverse momentum significance in the ATLAS Detector*, ATLAS-CONF-2018-038, 2018, URL: <https://cds.cern.ch/record/2630948>.
- [25] ATLAS Collaboration, *Search for a scalar partner of the top quark in the all-hadronic $t\bar{t}$ plus missing transverse momentum final state at $\sqrt{s}=13$ TeV with the ATLAS detector*, (2020), arXiv: [2004.14060 \[hep-ex\]](#).
- [26] ATLAS Collaboration, *Search for new phenomena with top quark pairs in final states with one lepton, jets, and missing transverse momentum in pp collisions at $\sqrt{s} = 13$ TeV with the ATLAS detector*, ATLAS-CONF-2020-003, 2020, URL: <https://cds.cern.ch/record/2711489>.
- [27] ATLAS Collaboration, *ATLAS Run 1 searches for direct pair production of third-generation squarks at the Large Hadron Collider*, *Eur. Phys. J. C* **75** (2015) 510, arXiv: [1506.08616 \[hep-ex\]](#).
- [28] ATLAS Collaboration, *Search for a scalar partner of the top quark in the jets plus missing transverse momentum final state at $\sqrt{s} = 13$ TeV with the ATLAS detector*, *JHEP* **12** (2017) 085, arXiv: [1709.04183 \[hep-ex\]](#).
- [29] ATLAS Collaboration, *Search for top-squark pair production in final states with one lepton, jets, and missing transverse momentum using 36fb^{-1} of $\sqrt{s} = 13$ TeV pp collision data with the ATLAS detector*, *JHEP* **06** (2018) 108, arXiv: [1711.11520 \[hep-ex\]](#).
- [30] ATLAS Collaboration, *Search for supersymmetry in final states with charm jets and missing transverse momentum in 13 TeV pp collisions with the ATLAS detector*, *JHEP* **09** (2018) 050, arXiv: [1805.01649 \[hep-ex\]](#).
- [31] ATLAS Collaboration, *Search for dark matter and other new phenomena in events with an energetic jet and large missing transverse momentum using the ATLAS detector*, *JHEP* **01** (2018) 126, arXiv: [1711.03301 \[hep-ex\]](#).
- [32] ATLAS Collaboration, *Measurements of top-quark pair spin correlations in the $e\mu$ channel at $\sqrt{s} = 13$ TeV using pp collisions in the ATLAS detector*, (2019), arXiv: [1903.07570 \[hep-ex\]](#).
- [33] CMS Collaboration, *Inclusive search for supersymmetry using razor variables in pp collisions at $\sqrt{s} = 13$ TeV*, *Phys. Rev. D* **95** (2017) 012003, arXiv: [1609.07658 \[hep-ex\]](#).
- [34] CMS Collaboration, *A search for new phenomena in pp collisions at $\sqrt{s} = 13$ TeV in final states with missing transverse momentum and at least one jet using the α_T variable*, *Eur. Phys. J. C* **77** (2017) 294, arXiv: [1611.00338 \[hep-ex\]](#).
- [35] CMS Collaboration, *Searches for pair production of third-generation squarks in $\sqrt{s} = 13$ TeV pp collisions*, *Eur. Phys. J. C* **77** (2017) 327, arXiv: [1612.03877 \[hep-ex\]](#).
- [36] CMS Collaboration, *Search for direct production of supersymmetric partners of the top quark in the all-jets final state in proton–proton collisions at $\sqrt{s} = 13$ TeV*, *JHEP* **10** (2017) 005, arXiv: [1707.03316 \[hep-ex\]](#).
- [37] CMS Collaboration, *Search for top squark pair production in pp collisions at $\sqrt{s} = 13$ TeV using single lepton events*, *JHEP* **10** (2017) 019, arXiv: [1706.04402 \[hep-ex\]](#).

- [38] CMS Collaboration, *Search for top squarks and dark matter particles in opposite-charge dilepton final states at $\sqrt{s} = 13$ TeV*, *Phys. Rev. D* **97** (2018) 032009, arXiv: 1711.00752 [hep-ex].
- [39] CMS Collaboration, *Searches for physics beyond the standard model with the M_{T2} variable in hadronic final states with and without disappearing tracks in proton–proton collisions at $\sqrt{s} = 13$ TeV*, *Eur. Phys. J. C* **80** (2020) 3, arXiv: 1909.03460 [hep-ex].
- [40] CMS Collaboration, *Search for supersymmetry in proton–proton collisions at 13 TeV in final states with jets and missing transverse momentum*, *JHEP* **10** (2019) 244, arXiv: 1908.04722 [hep-ex].
- [41] A. M. Sirunyan et al., *Search for direct top squark pair production in events with one lepton, jets, and missing transverse momentum at 13 TeV with the CMS experiment*, *JHEP* **05** (2020) 032, arXiv: 1912.08887 [hep-ex].
- [42] CMS Collaboration, *Search for Dark Matter Particles Produced in Association with a Top Quark Pair at $\sqrt{s} = 13$ TeV*, *Phys. Rev. Lett.* **122** (2019) 011803, arXiv: 1807.06522 [hep-ex].
- [43] ATLAS Collaboration, *The ATLAS Experiment at the CERN Large Hadron Collider*, *JINST* **3** (2008) S08003.
- [44] ATLAS Collaboration, *ATLAS Insertable B-Layer Technical Design Report*, ATLAS-TDR-19, 2010, URL: <https://cds.cern.ch/record/1291633>, *ATLAS Insertable B-Layer Technical Design Report Addendum*, ATLAS-TDR-19-ADD-1, 2012, URL: <https://cds.cern.ch/record/1451888>.
- [45] B. Abbott et al., *Production and integration of the ATLAS Insertable B-Layer*, *JINST* **13** (2018) T05008, arXiv: 1803.00844 [physics.ins-det].
- [46] ATLAS Collaboration, *Performance of the ATLAS trigger system in 2015*, *Eur. Phys. J. C* **77** (2017) 317, arXiv: 1611.09661 [hep-ex].
- [47] ATLAS Collaboration, *Luminosity determination in pp collisions at $\sqrt{s} = 13$ TeV using the ATLAS detector at the LHC*, ATLAS-CONF-2019-021, 2019, URL: <https://cds.cern.ch/record/2677054>.
- [48] G. Avoni et al., *The new LUCID-2 detector for luminosity measurement and monitoring in ATLAS*, *JINST* **13** (2018) P07017.
- [49] ATLAS Collaboration, *Performance of the missing transverse momentum triggers for the ATLAS detector during Run-2 data taking*, (2020), arXiv: 2005.09554 [hep-ex].
- [50] S. Agostinelli et al., *GEANT4 – a simulation toolkit*, *Nucl. Instrum. Meth. A* **506** (2003) 250.
- [51] ATLAS Collaboration, *The ATLAS Simulation Infrastructure*, *Eur. Phys. J. C* **70** (2010) 823, arXiv: 1005.4568 [physics.ins-det].
- [52] ATLAS Collaboration, *Electron and photon performance measurements with the ATLAS detector using the 2015–2017 LHC proton–proton collision data*, *JINST* **14** (2019) P12006, arXiv: 1908.00005 [hep-ex].
- [53] ATLAS Collaboration, *Muon reconstruction performance of the ATLAS detector in proton–proton collision data at $\sqrt{s} = 13$ TeV*, *Eur. Phys. J. C* **76** (2016) 292, arXiv: 1603.05598 [hep-ex].
- [54] ATLAS Collaboration, *ATLAS b-jet identification performance and efficiency measurement with $t\bar{t}$ events in pp collisions at $\sqrt{s} = 13$ TeV*, *Eur. Phys. J. C* **79** (2019) 970, arXiv: 1907.05120 [hep-ex].

- [55] J. Alwall et al., *The automated computation of tree-level and next-to-leading order differential cross sections, and their matching to parton shower simulations*, *JHEP* **07** (2014) 079, arXiv: [1405.0301 \[hep-ph\]](#).
- [56] T. Sjöstrand, S. Mrenna and P. Z. Skands, *A brief introduction to PYTHIA 8.1*, *Comput. Phys. Commun.* **178** (2008) 852, arXiv: [0710.3820 \[hep-ph\]](#).
- [57] P. Artoisenet, R. Frederix, O. Mattelaer and R. Rietkerk, *Automatic spin-entangled decays of heavy resonances in Monte Carlo simulations*, *JHEP* **03** (2013) 015, arXiv: [1212.3460 \[hep-ph\]](#).
- [58] J. Debove, B. Fuks and M. Klasen, *Threshold resummation for gaugino pair production at hadron colliders*, *Nucl. Phys. B* **842** (2011) 51, arXiv: [1005.2909 \[hep-ph\]](#).
- [59] B. Fuks, M. Klasen, D. R. Lamprea and M. Rothering, *Gaugino production in proton-proton collisions at a center-of-mass energy of 8 TeV*, *JHEP* **10** (2012) 081, arXiv: [1207.2159 \[hep-ph\]](#).
- [60] B. Fuks, M. Klasen, D. R. Lamprea and M. Rothering, *Precision predictions for electroweak superpartner production at hadron colliders with Resummino*, *Eur. Phys. J. C* **73** (2013) 2480, arXiv: [1304.0790 \[hep-ph\]](#).
- [61] J. Fiaschi and M. Klasen, *Neutralino-chargino pair production at NLO+NLL with resummation-improved parton density functions for LHC Run II*, *Phys. Rev. D* **98** (2018) 055014, arXiv: [1805.11322 \[hep-ph\]](#).
- [62] G. Bozzi, B. Fuks and M. Klasen, *Threshold Resummation for Slepton-Pair Production at Hadron Colliders*, *Nucl. Phys. B* **777** (2007) 157, arXiv: [hep-ph/0701202 \[hep-ph\]](#).
- [63] B. Fuks, M. Klasen, D. R. Lamprea and M. Rothering, *Revisiting slepton pair production at the Large Hadron Collider*, *JHEP* **01** (2014) 168, arXiv: [1310.2621 \[hep-ph\]](#).
- [64] J. Fiaschi and M. Klasen, *Slepton pair production at the LHC in NLO+NLL with resummation-improved parton densities*, *JHEP* **03** (2018) 094, arXiv: [1801.10357 \[hep-ph\]](#).
- [65] C. Borschensky et al., *Squark and gluino production cross sections in pp collisions at $\sqrt{s} = 13, 14, 33$ and 100 TeV*, *Eur. Phys. J. C* **74** (2014) 3174, arXiv: [1407.5066 \[hep-ph\]](#).
- [66] L. Lönnblad and S. Prestel, *Merging multi-leg NLO matrix elements with parton showers*, *JHEP* **03** (2013) 166, arXiv: [1211.7278 \[hep-ph\]](#).
- [67] ATLAS Collaboration, *ATLAS Pythia 8 tunes to 7 TeV data*, ATL-PHYS-PUB-2014-021, 2014, URL: <https://cds.cern.ch/record/1966419>.
- [68] R. D. Ball et al., *Parton distributions with LHC data*, *Nucl. Phys. B* **867** (2013) 244, arXiv: [1207.1303 \[hep-ph\]](#).
- [69] T. Sjöstrand et al., *An introduction to PYTHIA 8.2*, *Comput. Phys. Commun.* **191** (2015) 159, arXiv: [1410.3012 \[hep-ph\]](#).
- [70] O. Mattelaer and E. Vryonidou, *Dark matter production through loop-induced processes at the LHC: the s-channel mediator case*, *Eur. Phys. J. C* **75** (2015) 436, arXiv: [1508.00564 \[hep-ph\]](#).
- [71] M. Backović et al., *Higher-order QCD predictions for dark matter production at the LHC in simplified models with s-channel mediators*, *Eur. Phys. J. C* **75** (2015) 482, arXiv: [1508.05327 \[hep-ph\]](#).
- [72] D. J. Lange, *The EvtGen particle decay simulation package*, *Nucl. Instrum. Meth. A* **462** (2001) 152.
- [73] ATLAS Collaboration, *The Pythia 8 A3 tune description of ATLAS minimum bias and inelastic measurements incorporating the Donnachie–Landshoff diffractive model*, ATL-PHYS-PUB-2016-017, 2016, URL: <https://cds.cern.ch/record/2206965>.

- [74] S. Frixione, P. Nason and C. Oleari, *Matching NLO QCD computations with parton shower simulations: the POWHEG method*, *JHEP* **11** (2007) 070, arXiv: [0709.2092 \[hep-ph\]](#).
- [75] S. Alioli, P. Nason, C. Oleari and E. Re, *A general framework for implementing NLO calculations in shower Monte Carlo programs: the POWHEG BOX*, *JHEP* **06** (2010) 043, arXiv: [1002.2581 \[hep-ph\]](#).
- [76] P. Nason, *A new method for combining NLO QCD with shower Monte Carlo algorithms*, *JHEP* **11** (2004) 040, arXiv: [hep-ph/0409146](#).
- [77] M. Czakon and A. Mitov, *Top++: A program for the calculation of the top-pair cross-section at hadron colliders*, *Comput. Phys. Commun.* **185** (2014) 2930, arXiv: [1112.5675 \[hep-ph\]](#).
- [78] R. D. Ball et al., *Parton distributions for the LHC Run II*, *JHEP* **04** (2015) 040, arXiv: [1410.8849 \[hep-ph\]](#).
- [79] ATLAS Collaboration, *Modelling of the $t\bar{t}H$ and $t\bar{t}V$ ($V = W, Z$) processes for $\sqrt{s} = 13$ TeV ATLAS analyses*, ATL-PHYS-PUB-2016-005, 2016, URL: <https://cds.cern.ch/record/2120826>.
- [80] H. B. Hartanto, B. Jager, L. Reina and D. Wackeroth, *Higgs boson production in association with top quarks in the POWHEG BOX*, *Phys. Rev. D* **91** (2015) 094003, arXiv: [1501.04498 \[hep-ph\]](#).
- [81] R. Frederix, E. Re and P. Torrielli, *Single-top t -channel hadroproduction in the four-flavour scheme with POWHEG and aMC@NLO*, *JHEP* **09** (2012) 130, arXiv: [1207.5391 \[hep-ph\]](#).
- [82] S. Alioli, P. Nason, C. Oleari and E. Re, *NLO single-top production matched with shower in POWHEG: s - and t -channel contributions*, *JHEP* **09** (2009) 111, arXiv: [0907.4076 \[hep-ph\]](#).
- [83] M. Aliev et al., *HATHOR - HAdronic Top and Heavy quarks crOss section calculatoR*, *Comput. Phys. Commun.* **182** (2011) 1034, arXiv: [1007.1327 \[hep-ph\]](#).
- [84] P. Kant et al., *HATHOR for single top-quark production: Updated predictions and uncertainty estimates for single top-quark production in hadronic collisions*, *Comput. Phys. Commun.* **191** (2015) 74, arXiv: [1406.4403 \[hep-ph\]](#).
- [85] N. Kidonakis, *Next-to-next-to-leading-order collinear and soft gluon corrections for t -channel single top quark production*, *Phys. Rev. D* **83** (2011) 091503, arXiv: [1103.2792 \[hep-ph\]](#).
- [86] N. Kidonakis, *Two-loop soft anomalous dimensions for single top quark associated production with a W - or H -*, *Phys. Rev. D* **82** (2010) 054018, arXiv: [1005.4451 \[hep-ph\]](#).
- [87] N. Kidonakis, *NNLL resummation for s -channel single top quark production*, *Phys. Rev. D* **81** (2010) 054028, arXiv: [1001.5034 \[hep-ph\]](#).
- [88] T. Gleisberg et al., *Event generation with SHERPA 1.1*, *JHEP* **02** (2009) 007, arXiv: [0811.4622 \[hep-ph\]](#).
- [89] ATLAS Collaboration, *Monte Carlo Generators for the Production of a W or Z/γ^* Boson in Association with Jets at ATLAS in Run 2*, ATL-PHYS-PUB-2016-003, 2016, URL: <https://cds.cern.ch/record/2120133>.
- [90] R. Gavin, Y. Li, F. Petriello and S. Quackenbush, *FEWZ 2.0: A code for hadronic Z production at next-to-next-to-leading order*, (2010) 2388, arXiv: [1011.3540 \[hep-ph\]](#).
- [91] ATLAS Collaboration, *Multi-Boson Simulation for 13 TeV ATLAS Analyses*, ATL-PHYS-PUB-2017-005, 2017, URL: <https://cds.cern.ch/record/2261933>.
- [92] ATLAS Collaboration, *Topological cell clustering in the ATLAS calorimeters and its performance in LHC Run 1*, *Eur. Phys. J. C* **77** (2017) 490, arXiv: [1603.02934 \[hep-ex\]](#).

- [93] M. Cacciari, G. P. Salam and G. Soyez, *The anti- k_t jet clustering algorithm*, **JHEP** **04** (2008) 063, arXiv: [0802.1189 \[hep-ph\]](#).
- [94] M. Cacciari, G. P. Salam and G. Soyez, *FastJet user manual*, **Eur. Phys. J. C** **72** (2012) 1896, arXiv: [1111.6097 \[hep-ph\]](#).
- [95] ATLAS Collaboration, *Jet energy scale measurements and their systematic uncertainties in proton–proton collisions at $\sqrt{s} = 13$ TeV with the ATLAS detector*, **Phys. Rev. D** **96** (2017) 072002, arXiv: [1703.09665 \[hep-ex\]](#).
- [96] ATLAS Collaboration, *Tagging and suppression of pileup jets with the ATLAS detector*, ATLAS-CONF-2014-018, 2014, URL: <https://cds.cern.ch/record/1700870>.
- [97] ATLAS Collaboration, *Selection of jets produced in 13 TeV proton–proton collisions with the ATLAS detector*, ATLAS-CONF-2015-029, 2015, URL: <https://cds.cern.ch/record/2037702>.
- [98] ATLAS Collaboration, *Performance of pile-up mitigation techniques for jets in pp collisions at $\sqrt{s} = 8$ TeV using the ATLAS detector*, **Eur. Phys. J. C** **76** (2016) 581, arXiv: [1510.03823 \[hep-ex\]](#).
- [99] ATLAS Collaboration, *Performance of missing transverse momentum reconstruction with the ATLAS detector using proton–proton collisions at $\sqrt{s} = 13$ TeV*, **Eur. Phys. J. C** **78** (2018) 903, arXiv: [1802.08168 \[hep-ex\]](#).
- [100] C. G. Lester and D. J. Summers, *Measuring masses of semi-invisibly decaying particles pair produced at hadron colliders*, **Phys. Lett. B** **463** (1999) 99, arXiv: [hep-ph/9906349](#).
- [101] A. Barr, C. G. Lester and P. Stephens, *A variable for measuring masses at hadron colliders when missing energy is expected; m_{T2} : the truth behind the glamour*, **J. Phys. G** **29** (2003) 2343, arXiv: [hep-ph/0304226](#).
- [102] W. S. Cho, K. Choi, Y. G. Kim and C. B. Park, *Measuring superparticle masses at hadron collider using the transverse mass kink*, **JHEP** **02** (2008) 035, arXiv: [0711.4526 \[hep-ph\]](#).
- [103] M. Burns, K. Kong, K. T. Matchev and M. Park, *Using subsystem M_{T2} for complete mass determinations in decay chains with missing energy at hadron colliders*, **JHEP** **03** (2009) 143, arXiv: [0810.5576 \[hep-ph\]](#).
- [104] M. R. Buckley, J. D. Lykken, C. Rogan and M. Spiropulu, *Super-razor and searches for sleptons and charginos at the LHC*, **Phys. Rev. D** **89** (2014) 055020, arXiv: [1310.4827 \[hep-ph\]](#).
- [105] G. Cowan, K. Cranmer, E. Gross and O. Vitells, *Asymptotic formulae for likelihood-based tests of new physics*, **Eur. Phys. J. C** **71** (2011) 1554, arXiv: [1007.1727 \[physics.data-an\]](#), Erratum: **Eur. Phys. J. C** **73** (2013) 2501.
- [106] M. Baak et al., *HistFitter software framework for statistical data analysis*, **Eur. Phys. J. C** **75** (2015) 153, arXiv: [1410.1280 \[hep-ex\]](#).
- [107] L. Heinrich, M. Feickert and G. Stark, *pyhf*, version 0.4.4, URL: <https://github.com/scikit-hep/pyhf>.
- [108] ATLAS Collaboration, *Measurement of the WW cross section in $\sqrt{s} = 7$ TeV pp collisions with ATLAS*, **Phys. Rev. Lett.** **107** (2011) 041802, arXiv: [1104.5225 \[hep-ex\]](#).
- [109] ATLAS Collaboration, *Search for anomalous production of prompt same-sign lepton pairs and pair-produced doubly charged Higgs bosons with $\sqrt{s} = 8$ TeV pp collisions using the ATLAS detector*, **JHEP** **03** (2015) 041, arXiv: [1412.0237 \[hep-ex\]](#).

- [110] S. Rettie, *Searches for new phenomena in leptonic final states using the ATLAS detector*, (2018), arXiv: [1810.00030 \[hep-ex\]](#).
- [111] CMS Collaboration, *Search for charged Higgs bosons with the $H^\pm \rightarrow \tau^\pm \nu_\tau$ decay channel in proton-proton collisions at $\sqrt{s} = 13$ TeV*, *JHEP* **07** (2019) 142, arXiv: [1903.04560 \[hep-ex\]](#).
- [112] CMS Collaboration, *Search for singly produced third-generation leptoquarks decaying to a τ lepton and a b quark in proton-proton collisions at $\sqrt{s} = 13$ TeV*, *JHEP* **07** (2018) 115, arXiv: [1806.03472 \[hep-ex\]](#).
- [113] ATLAS Collaboration, *Jet Calibration and Systematic Uncertainties for Jets Reconstructed in the ATLAS Detector at $\sqrt{s} = 13$ TeV*, ATL-PHYS-PUB-2015-015, 2015, URL: <https://cds.cern.ch/record/2037613>.
- [114] ATLAS Collaboration, *Calibration of b -tagging using dileptonic top pair events in a combinatorial likelihood approach with the ATLAS experiment*, ATLAS-CONF-2014-004, 2014, URL: <https://cds.cern.ch/record/1664335>.
- [115] ATLAS Collaboration, *Calibration of the performance of b -tagging for c and light-flavour jets in the 2012 ATLAS data*, ATLAS-CONF-2014-046, 2014, URL: <https://cds.cern.ch/record/1741020>.
- [116] ATLAS Collaboration, *Performance of electron and photon triggers in ATLAS during LHC Run 2*, *Eur. Phys. J. C* **80** (2020) 47, arXiv: [1909.00761 \[hep-ex\]](#).
- [117] ATLAS Collaboration, *Performance of the ATLAS muon triggers in Run 2*, arXiv e-prints, arXiv:2004.13447 (2020) arXiv:2004.13447, arXiv: [2004.13447 \[hep-ex\]](#).
- [118] ATLAS Collaboration, *Expected performance of missing transverse momentum reconstruction for the ATLAS detector at $\sqrt{s} = 13$ TeV*, ATL-PHYS-PUB-2015-023, 2015, URL: <https://cds.cern.ch/record/2037700>.
- [119] ATLAS Collaboration, *Simulation of top-quark production for the ATLAS experiment at $\sqrt{s} = 13$ TeV*, ATL-PHYS-PUB-2016-004, 2016, URL: <https://cds.cern.ch/record/2120417>.
- [120] ATLAS Collaboration, *Improvements in $t\bar{t}$ modelling using NLO+PS Monte Carlo generators for Run 2*, ATL-PHYS-PUB-2018-009, 2018, URL: <https://cds.cern.ch/record/2630327>.
- [121] ATLAS Collaboration, *Modelling of the $t\bar{t}H$ and $t\bar{t}V$ ($V = W, Z$) processes for $\sqrt{s} = 13$ TeV ATLAS analyses*, ATL-PHYS-PUB-2015-022, 2016, URL: <http://cds.cern.ch/record/2120826>.
- [122] ATLAS Collaboration, *Measurement of the $t\bar{t}Z$ and $t\bar{t}W$ cross sections in proton–proton collisions at $\sqrt{s} = 13$ TeV with the ATLAS detector*, *Phys. Rev. D* **99** (2019) 072009, arXiv: [1901.03584 \[hep-ex\]](#).
- [123] S. Frixione, E. Laenen, P. Motylinski, C. D. White and B. R. Webber, *Single-top hadroproduction in association with a W boson*, *JHEP* **07** (2008) 029, arXiv: [0805.3067 \[hep-ph\]](#).
- [124] O. Bessidskaia Bylund, ‘Modelling Wt and tWZ production at NLO for ATLAS analyses’, *9th International Workshop on Top Quark Physics*, 2016, arXiv: [1612.00440 \[hep-ph\]](#).
- [125] J. Butterworth et al., *PDF4LHC recommendations for LHC Run II*, *J. Phys. G* **43** (2016) 023001, arXiv: [1510.03865 \[hep-ph\]](#).
- [126] R. D. Cousins, J. T. Linnemann and J. Tucker, *Evaluation of three methods for calculating statistical significance when incorporating a systematic uncertainty into a test of the background-only hypothesis for a Poisson process*, *Nucl. Instrum. Meth. A* **595** (2008) 480, arXiv: [physics/0702156 \[physics.data-an\]](#).

- [127] A. L. Read, *Presentation of search results: the CL_S technique*, [J. Phys. G](#) **28** (2002) 2693.

Appendix

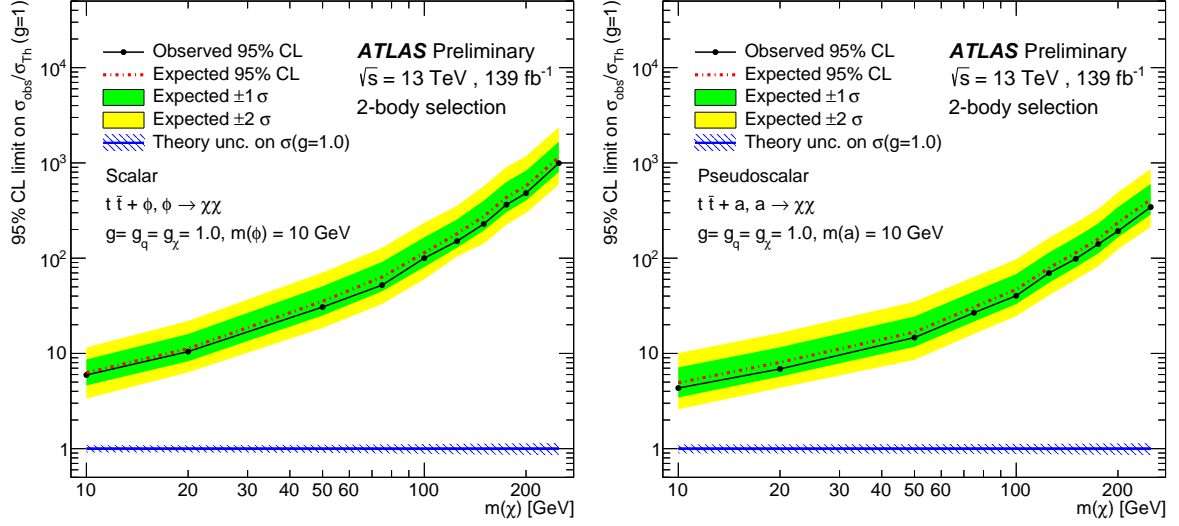


Figure 16: Exclusion limits for $t\bar{t} + \phi$ scalar (left figure) and $t\bar{t} + a$ pseudoscalar (right figure) models as a function of the DM particle mass for a mediator mass of 10 GeV. The limits are calculated at 95% CL and are expressed in terms of the ratio of the excluded cross-section to the nominal cross-section for a coupling assumption of $g = g_q = g_\chi = 1$. The solid (dashed) lines show the observed (expected) exclusion limits.